Tunable Optical Molecular Thermometers Based on Metallacrowns

Elvin Salerno, Albano Carneiro Neto, Svetlana Eliseeva, Miguel Hernández-Rodríguez, Jacob Lutter, Timothée Lathion, Jeff Kampf, Stéphane Petoud, Luis Carlos, Vincent Pecoraro

To cite this version:

Elvin Salerno, Albano Carneiro Neto, Svetlana Eliseeva, Miguel Hernández-Rodríguez, Jacob Lutter, et al.. Tunable Optical Molecular Thermometers Based on Metallacrowns. Journal of the American Chemical Society, 2022, 144 (40), pp.18259-18271. 10.1021/jacs.2c04821 . hal-04040491

HAL Id: hal-04040491

https://hal.science/hal-04040491v1

Submitted on 22 Mar 2023

Tunable Optical Molecular Thermometers Based on Metallacrowns

Elvin V. Salerno,† Albano N. Carneiro Neto,# Svetlana V. Eliseeva,*,‡ Miguel A. Hernández-Rodríguez,# Jacob C. Lutter,† Timothée Lathion,† Jeff W. Kampf,† Stéphane Petoud, *,‡ Luis D. Carlos, *,# and Vincent L. Pecoraro*,†

† Department of Chemistry, Willard H. Dow Laboratories, University of Michigan, Ann Arbor, Michigan, United States, 48109. *Email: V. L. Pecoraro, vlpec@umich.edu.

Phantom-g, CICECO-Aveiro Institute of Materials, Department of Physics, University of Aveiro Campus de Santiago, Aveiro, Portugal, 3810-193. *Email: L. D. Carlos, lcarlos@ua.pt

‡ Centre de Biophysique Moléculaire CNRS UPR 4301, 45071 Orléans Cedex 2, France. *E-mails: S. V. Eliseeva, svetlana.eliseeva@cnrs-orleans.fr; S. Petoud, stephane.petoud@inserm.fr

---

Abstract. The effect of ligands' energy levels on thermal dependence of lanthanide emission was examined to create new molecular nanothermometers. A series of $Ln_2Ga_8L'_8L''_4$ metallacrowns (shorthand $Ln_2L'_8$), where Ln = Gd^{3+}, Tb^{3+}, or Sm^{3+}; H_3L' = salicylhydroxamic acid (H_3shi), 5-methylsalicylhydroxamic acid (H_3mshi), 5-methoxysalicylhydroxamic acid (H_3moshi), and 3-hydroxy-2-naphthohydroxamic acid (H_3nha); and H_2L'' = isophthalic acid (H_2iph) was synthesized and characterized. Within the series, ligand-centered singlet state (S_1) energy levels ranged from 23300 to 27800 cm^{-1}, while triplet (T_1) energy levels ranged from 18150 to 21980 cm^{-1}. We demonstrated that the difference between T_1 levels and relevant energies of the excited $^4G_{5/2}$ level of Sm^{3+} (17800 cm^{-1}) and $^5D_4$ level of Tb^{3+} (20400 cm^{-1}) is the major parameter controlling thermal dependence of the emission intensity via the back energy transfer mechanism. However, when the energy difference between S_1 and T_1 levels is small (below 3760 cm^{-1}), the $S_1 \rightarrow T_1$ intersystem crossing (and its reverse, $S_1 \leftarrow T_1$) mechanism contributes to the thermal behavior of metallacrowns. Both mechanisms affect Ln^{3+}-centered room-temperature quantum yields with values ranging from 2.07(6) to 31.2(2) % for $Tb_2L'_8$ and from 0.0267(7) to 2.27(5) % for $Sm_2L'_8$. The maximal thermal dependence varies over a wide thermal range (ca. 150–350 K), based on energy gaps between relevant ligand-based and lanthanide-based electronic states. By mixing Tb_2moshi'$_8$ with Sm_2moshi'$_8$ in a 1:1 ratio an optical thermometer with a relative thermal sensitivity larger than 3 %/K at 225 K was created. Other temperature ranges are also accessible with this approach.

INTRODUCTION

Understanding thermal dynamics is essential for the analysis and engineering of almost any physical system. Temperature has long been an important scientific measurement, with established thermometry techniques such as mercury-based pressure gauges or voltage-based thermocouples.[1] Optical thermometers are gaining an increasing interest as they provide a unique means for the non-contact detection of the temperature of a target. For example, pyrometry-based methods analyze the properties of the emitted infrared radiation from a system to determine thermal parameters, with applications such as infrared temperature guns or determination of the temperature of distant stars.[2,3]

Optical thermometry methods are often the basis for the up-and-coming generation of thermometers known as nanothermometers.[4] Nanothermometry is the measurement of temperature at the submicron level. As we seek to understand the physical basis of many systems from the ground up, nanothermometry becomes increasingly important. This field has a plethora of uses such as the analysis of microelectronics,[5] cellular biology,[6] nanomedicine,[7,8] or microfluidics[9] for which traditional methods of thermometry are not amenable.

An optical nanothermometer correlates a temperature value with the change in photophysical properties of a probe. Two schemes used involve observing changes in luminescence lifetimes or emission intensities in response to temperature. Lifetime-based techniques are functional and can be quite sensitive, but rely on specialized equipment, rigorous data analysis methodologies, have long acquisition times that preclude dynamic measurements shorter than the lifetime of the probe, and are ineffective for short-timescale thermal mapping.[10] Ratiometric intensity-based measurements are another promising approach. This technique correlates the temperature with the ratio between the integrated intensities of two different emission bands, Δ.[11] A ratiometric approach, rather than the intensity measurement of a single transition, is necessary to avoid artifacts coming from parameters besides temperature such as probe concentration or signal attenuation. Ratiometric probes can be based on a single compound,[12–14] or on a combination of two compounds.[10,15]

Solid-state and molecular materials can be used to create nanothermometric devices. Some prominent probes include nitrogen-vacancy nanodiamonds,[16,17] organic fluorophores,[18,19] metal-organic frameworks[20,21], metal-coordinating molecules,[22,23] or nanoparticles.[24,25] Lanthanide(III)-based thermometry probes have inherently attractive properties due to the buried nature of 4f valence orbitals. In particular, properties including: (i) long-lived emission lifetimes which can be used to dodge background fluorescence via time-gated experiments,[26] and (ii) sharp emission bands with fixed (or minimally affected) positions of the barycenters that can be easily distinguished from background fluorescence.[27] In solid-state systems such as in metal-organic frameworks or in lanthanide-doped nanoparticles, the change in emission intensities is often induced by thermally-dependent energy transfer between two different lanthanide(III) ions (Ln^{3+}).[28] Many sensitive nanothermometric systems that benefit from this principle have been created.[11,20,21,29–35] However, their design requires a close proximity between the Ln^{3+} to ensure energy transfer. Moreover, the modulation of functional properties of solid-state systems might be challenging and restricted by the limited choice of available methodologies.

Molecular nanothermometers are desirable because of their functional properties, for example, their sensitivity and thermal response range,[36] biocompatibility[37,38] and surface binding,[39] can be tuned by chemical modifications.

Molecular thermometers are typically either all-organic fluorophores or metal-coordinating complexes. Organic fluorophores have drawbacks such as broad emissive bands with short luminescence lifetimes that cannot always be differentiated from background fluorescence, particularly in biological thermal imaging applications where autofluorescence contribution is significant. In metal-coordinating organic complexes, coordinated metals are usually d-transition metal ions, such as Cu^{2+},[40–42] or Ln^{3+} ions.[5,22,31] There are promising d-transition metal systems, but these can suffer from limitations similar to the ones of organic fluorophores where their response is not tunable for use across a wide-range of temperatures.

Ln^{3+}-based molecular complexes offer the above-mentioned benefits such as sharp emission bands and long luminescence lifetimes. However, free Ln^{3+} suffer from very weak absorbance due to the parity-forbidden nature of most f–f transitions.[43] This weak absorptivity of Ln^{3+} ions can be overcome by a sensitization through an appropriate ligand via the "antennae effect".[44] Studies have shown that the energy positions of the excited singlet (S_1) and triplet (T_1) states of the ligand relative to the accepting energy level of the Ln^{3+} level play an important role in the sensitization of Ln^{3+} in such compounds,[45–49] and can play a role in thermal dependence of emission intensity.[50,51] Ideally, the electronic states of the ligand should be higher in energy than, and close enough to, the accepting Ln^{3+} energy state to permit adequate energy transfer, but not too close to prevent a back energy transfer from the Ln^{3+} to the ligand. The thermal response of Ln^{3+} emission can also be tuned via interaction with the ligand field to increase the thermal sensitivity[52] or to change the range of thermal activity.[36] Some sensitive Ln^{3+}-based thermometers have been constructed, but a strategy for rational tuning of a high sensitivity Ln^{3+}-based molecular system for use across a wide range of temperatures is currently missing.

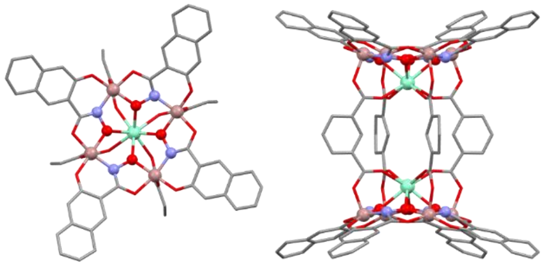

Figure 1. Top-down (left) and side-on (right) views of the Ln_2nha_8 complex. The structure is a dimer of two 12-MC-4 MC units linked by four isophthalic acid bridges. The Ln[– Ga^{3+}–N–O–]$_4$ motif is highlighted. Color code: Ga, pink; Ln, green; O, red; N, blue; C, grey. Solvents, counter cations, and hydrogen atoms are omitted for clarity. This structure was obtained on X-ray single crystal diffraction on the Sm^{3+} analogue.

Herein we present a series of molecular nanothermometers based on dimeric metallacrowns (MCs) with the general composition $Ln_2Ga_8L'_8L''_4$ (shorthand $Ln_2L'_8$), where Ln^{3+} = Gd^{3+}, Tb^{3+}, or Sm^{3+}; H_3L' = salicylhydroxamic acid (H_3shi), 5-methylsalicylhydroxamic acid (H_3mshi), 5-methoxysalicylhydroxamic acid (H_3moshi), and 3-hydroxy-2-naphthohydroxamic acid (H_3nha); and H_2L'' = isophthalic acid (H_2iph) (**Figure 1**, center, right). Within the studied series of the $Ln_2L'_8$, the MC dimeric structures have similar topology (**Figure 1; Figure 2, left**), ensuring the similarity of the first coordination sphere around the Ln^{3+} ion. For the $Tb_2L'_8$ and $Sm_2L'_8$ MCs, photophysical properties were investigated in detail. Diffuse reflectance and Ln^{3+}-centered excitation spectra, luminescence lifetimes, quantum yields, as well as thermal dependence of emission spectra from ca. 11 to 400 K were acquired and analyzed. We have also studied the ligand-centered properties of the corresponding $Gd_2L'_8$ MCs to determine the energy positions of S_1 and T_1 levels. To assemble the $Ln_2L'_8$, MCs we have chosen sensitizing hydroxamate ligands that possess disparate S_1 and T_1 energy levels. In this manner, we have analyzed how the Ln*–T_1 and Ln*–S_1 energy gaps influence the thermal dependence of emission intensities. We rationalize these findings in a broader sense to describe how one can change the excited state energies of organic antennae to modify the range of the highest thermal sensitivity (ca. 11–400 K). The reported findings can also be relevant for further designs of Ln^{3+}-based molecular compounds with large quantum yields, because quantum yields can be directly dependent on Ln^{3+}-ligand back energy transfer.

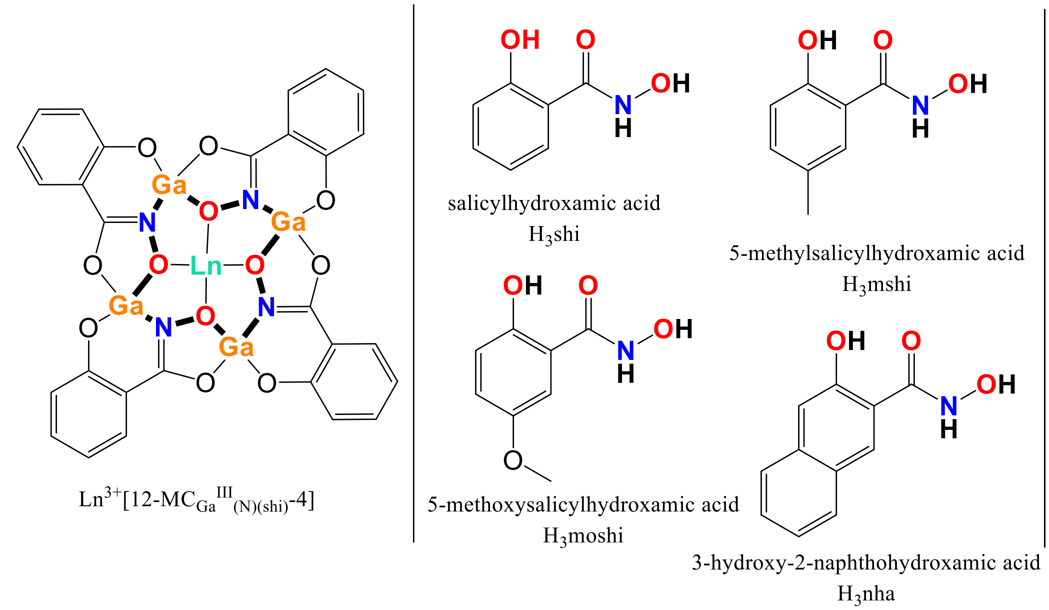

Figure 2. Left panel: schematic representation of a $Ln^{3+}[12\text{-}MC_{Ga^{III}(N)(shi)}\text{-}4]$ MC unit. The $-[Ga^{3+}-N-O]_4-$ ring motif is in bold. Center panel: representation of the four hydroxamic acids used in the present study, H_3L'. Each trianionic ligand forms analogous MC structures due to the identical binding motifs. Right panel: representation of the isophthalic acid, which acts as a bridging ligand and binds as iph^{2-} resulting in the formation of a dimeric structure as in 2. Binding atoms are presented in color.

EXPERIMENTAL SECTION

Synthesis

General synthetic considerations. All reagents and chemicals were purchased from commercial sources and used without further purification. All reactions were carried out aerobically under ambient conditions. Elemental analyses were performed by Atlantic Microlabs Inc. ESI-MS spectra were collected with an Agilent 6230 TOF HPLC-MS mass spectrometer in negative ion mode (–350V) on samples dissolved in methanol at a concentration of 2 mg/mL. ^1H NMR spectra were collected on a Varian MR400 NMR in deuterated DMSO at a concentration of 4 mg/mL.

Ln_2shi_8 complexes and N,3-dihydroxy-2-naphthamide (H_3nha) were prepared according to the previously reported procedures.[53,54]

Preparation of 5-methoxy salicylhydroxamic acid (H_3moshi). Potassium hydroxide (47.5 mmol) and hydroxylamine monohydrochloride (40 mmol) were combined in 20 mL of methanol and stirred for ten minutes over ice. A white precipitate (potassium chloride salt) formed. The precipitate was removed via vacuum filtration yielding a clear and colorless solution of hydroxylamine in methanol. To this stirred solution was added liquid methyl-5-methoxy salicylate (5 mmol). The solution immediately turned yellow. The solution was stirred for more than four days with a cap to prevent solvent loss. After four days, a clear orange solution was present. The pH was adjusted to ~1 with 2M aqueous HCl. Then 30 mL of water was added to precipitate a pale, orange solid. This solid was collected via vacuum filtration and washed with cold water. The clear/yellow filtrate was discarded. The solid was then triturated in methylene chloride, then collected via vacuum filtration. The precipitate was dried *in vacuo* to yield pure solid with 57.9% yield. ^{1}H NMR (400 mHz, DMSO-d_6) δ 11.75 (s, 1 H), 11.41 (s, 1 H), 9.33 (s, 1 H), 7.24 (d, J=3.1 Hz, 1 H), 7.00 (dd, J=9.0, 3.0 Hz, 1 H), 6.84 (d, J=9.0 Hz , 1 H), 3.71 (s, 3 H). Anal. Calcd. For $C_8H_9NO_4$: C, 52.46; H, 4.95; N, 7.65. Found: C, 52.33; H, 5.00; N, 7.45.

Preparation of 5-methyl salicylhydroxamic acid (H_3mshi). Potassium hydroxide (237.5 mmol) and hydroxylamine monohydrochloride (200 mmol) were combined in 100 mL of methanol and stirred for ten minutes over ice. A white precipitate (potassium chloride salt) formed. The precipitate was removed via vacuum filtration yielding a clear and colorless solution of hydroxylamine in methanol. To this stirred solution was added liquid methyl-5-methyl salicylate (5 mmol). The solution remains (initially) clear and colorless. The solution was stirred for more than seven days with a cap to prevent solvent loss. After seven days, a clear yellow solution was obtained. The pH was adjusted to ~1 with 2M aqueous HCl. Then 200 mL of water was added. The product was extracted with 4x50 mL portions of ethyl acetate. The solvent was removed via rotary evaporation. A small amount of yellow liquid and a pale white solid emerge. The solid was collected via filtration, rinsed with methylene chloride, then dried *in vacuo* to yield a pure solid with 56.5% yield. ^{1}H NMR (400 mHz, DMSO-d_6) δ 11.95 (s, 1 H), 11.34 (s, 1 H), 9.28 (s, 1 H), 7.50 (d, J=2.2 Hz, 1 H), 7.19 (dd, J=8.4, 2.2 Hz, 1 H), 6.80 (d, J=8.4 Hz, 1 H), 2.22 (s, 3 H). Anal. Calcd. For $C_8H_9NO_3$: C, 57.48; H, 5.43; N, 8.38. Found: C, 57.21; H, 5.54; N, 8.39.

Preparation of Ln_2moshi_8 complexes. 5-methoxy salicylhydroxamic acid (H_3moshi) (0.6 mmol), $Ln(NO_3)_3 \cdot xH_2O$ (0.15 mmol) (Ln^{3+} = Sm^{3+}, Gd^{3+}, Tb^{3+}), $Ga(NO_3)_3 \cdot xH_2O$ (0.6 mmol), and isophthalic acid (0.3 mmol) were dissolved in 30 mL of dimethyl formamide. A concentrated aqueous NaOH solution (19.87 M, 2.4 mmol) was added slowly and the solution was stirred for two hours under ambient condition. The solution was filtered, then the filtrate was left for slow evaporation, producing crystalline compound within 2–4 weeks. Compound was collected via filtration and dried *in vacuo*. A tan crystalline solid was collected in each case.

Sm_2moshi_8: $[Sm_2Ga_8(moshi)_8(iph)_4]Na_2 \cdot 5H_2O \cdot 8DMF$. Yield: 220 mg (84%). ESI-MS, calc. for $[M]^{2-}$, $Sm_2Ga_8C_{96}H_{64}N_8O_{48}$, 1477.3; found, 1477.2. Anal. Calcd. for $Sm_2Na_2Ga_8C_{111}H_{115}N_{13}O_{61}$: C, 39.20; H, 3.56; N, 6.09. Found: C, 39.05; H, 3.47; N, 6.33.

Gd_2moshi_8: $[Gd_2Ga_8(moshi)_8(iph)_4]Na_2 \cdot 5H_2O \cdot 8DMF$. Yield: 195 mg (74%). ESI-MS, calc. for $[M]^{2-}$, $Gd_2Ga_8C_{96}H_{64}N_8O_{48}$, 1484.3; found, 1484.2. Anal. Calcd. for $Gd_2Na_2Ga_8C_{111}H_{115}N_{13}O_{61}$: C, 39.05; H, 3.55; N, 6.07. Found: C, 39.01; H, 3.48; N, 6.03.

Tb_2moshi_8: $[Tb_2Ga_8(moshi)_8(iph)_4]Na_2 \cdot 5H_2O \cdot 8DMF$. Yield: 190 mg (72%). ESI-MS, calc. for $[M]^{2-}$, $Tb_2Ga_8C_{96}H_{64}N_8O_{48}$, 1486.3; found, 1486.2. Anal. Calcd. for $Tb_2Na_2Ga_8C_{111}H_{115}N_{13}O_{61}$: C, 39.01; H, 3.55; N, 6.07. Found: C, 38.90; H, 3.43; N, 6.14.

Preparation of Ln_2mshi_8 complexes. 5-methyl salicylhydroxamic acid (H_3mshi) (0.6 mmol), $Ln(NO_3)_3 \cdot xH_2O$ (0.15 mmol) (Ln^{3+} = Sm^{3+}, Gd^{3+}, Tb^{3+}), $Ga(NO_3)_3 \cdot xH_2O$ (0.6 mmol), and isophthalic acid (0.3 mmol) were dissolved in 30 mL of dimethyl formamide. A concentrated aqueous NaOH solution (19.87 M, 2.4 mmol) was added slowly and the resulting solution was stirred for two hours under ambient conditions. The solution was filtered and the filtrate was left for slow evaporation. After about 1 week, an amorphous, powdery precipitate appeared. The mixture was filtered again, and the filtrate was collected and again set for slow evaporation, producing crystalline compound within 2–3 weeks. A crystalline compound was collected via filtration and dried *in vacuo*. A pale white crystalline solid was collected in each case.

Sm_2mshi_8: $[Sm_2Ga_8(mshi)_8(iph)_4]Na_2 \cdot 10H_2O \cdot 10DMF$. Yield: 210 mg (74%). ESI-MS, calc. for $[M]^{2-}$, $Sm_2Ga_8C_{96}H_{64}N_8O_{40}$, 1413.8; found, 1413.3. Anal. Calcd. for $Sm_2Na_2Ga_8C_{126}H_{154}N_{18}O_{60}$: C, 39.98; H, 4.10; N, 6.66. Found: C, 40.10; H, 4.22; N, 6.66.

Gd_2mshi_8: $[Gd_2Ga_8(mshi)_8(iph)_4]Na_2 \cdot 10H_2O \cdot 9DMF$. Yield: 210 mg (75%). ESI-MS, calc. for $[M]^{2-}$, $Gd_2Ga_8C_{96}H_{64}N_8O_{40}$, 1421.3; found, 1420.3. Anal. Calcd. for $Gd_2Na_2Ga_8C_{123}H_{147}N_{17}O_{59}$: C, 39.65; H, 3.98; N, 6.40. Found: C, 39.66; H, 4.00; N, 6.38.

Tb_2mshi_8: $[Tb_2Ga_8(mshi)_8(iph)_4]Na_2 \cdot 8H_2O \cdot 10DMF$. Yield: 190 mg (67%). ESI-MS, calc. for $[M]^{2-}$, $Tb_2Ga_8C_{96}H_{64}N_8O_{40}$, 1422.3; found, 1422.3. Anal. Calcd. for $Tb_2Na_2Ga_8C_{126}H_{150}N_{18}O_{58}$: C, 40.18; H, 4.01; N, 6.69. Found: C, 40.22; H, 4.09; N, 6.55.

Preparation of Ln_2nha_8 complexes. $Ln(NO_3)_3 \cdot xH_2O$ (0.125 mmol) (Ln^{3+} = Sm^{3+}, Gd^{3+}, Tb^{3+}) and $Ga(NO_3)_3 \cdot xH_2O$ (0.5 mmol) were combined in 5 mL of dimethylformamide yielding to a clear and colorless solution. Separately, *N*,3-dihydroxy-2-naphthamide (H_3nha) (0.5 mmol) and isophthalic acid (0.25 mmol) were dissolved in 15 mL of dimethyl formamide, yielding a clear and yellow solution. To this solution, a concentrated aqueous NaOH solution (2.0 mmol) was added slowly and the solution was stirred for five minutes. Then, the two solutions were combined together and the resulting mixture was stirred for more than two hours under ambient conditions. The solution was filtered and the filtrate was left for slow evaporation, producing crystalline compound within 2–4 weeks. The compound was collected via filtration and dried *in vacuo*. A brown crystalline solid was collected in each case.

Sm_2nha_8: $[Sm_2Ga_8(nha)_8(iph)_4]Na_2 \cdot 14H_2O \cdot 14DMF$. Yield: 165 mg (59%). ESI-MS, calc. for $[M]^{2-}$, $Sm_2Ga_8C_{120}H_{64}N_8O_{40}$, 1558.8; found, 1558.8. Anal. Calcd. for $Sm_2Na_2Ga_8C_{162}H_{190}N_{22}O_{68}$: C, 43.84; H, 4.32; N, 6.94. Found: C, 43.93; H, 4.43; N, 6.94.

Gd_2nha_8: $[Gd_2Ga_8(nha)_8(iph)_4]Na_2 \cdot 12H_2O \cdot 11DMF$. Yield: 160 mg (61%). ESI-MS, calc. for $[M]^{2-}$, $Gd_2Ga_8C_{120}H_{64}N_8O_{40}$, 1564.8; found, 1564.8. Anal. Calcd. for $Gd_2Na_2Ga_8C_{153}H_{165}N_{19}O_{63}$: C, 43.80; H, 3.96; N, 6.34. Found: C, 43.79; H, 4.06; N, 6.22.

Tb_2nha_8: $[Tb_2Ga_8(nha)_8(iph)_4]Na_2 \cdot 15H_2O \cdot 12DMF$. Yield: 185 mg (68%). ESI-MS, calc. for $[M]^{2-}$, $Tb_2Ga_8C_{120}H_{64}N_8O_{40}$, 1567.3; found, 1566.8. Anal. Calcd. for $Tb_2Na_2Ga_8C_{156}H_{178}N_{20}O_{67}$: C, 43.38; H, 4.15; N, 6.49. Found: C, 43.48; H, 4.23; N, 6.49.

Crystallography. Single crystals were grown from a dimethylformamide/water solution of the compounds at room temperature. Crystals were mounted on a Rigaku AFC10K Saturn 944+ CCD-based X-ray diffractometer equipped with a low temperature device and Micromax-007HF Cu-target micro-focus rotating anode (λ = 1.54187 Å) operated at 1.2 kW power (40 kV, 30 mA). The X-ray intensities were measured at 85(1) K with the detector placed at a distance 42.00 mm from the crystal. d*trek images were exported to CrysAlisPro for processing and corrected for absorption.[55,56] The analysis of the data showed a negligible decay during the data collection. The structures of Sm_2nha_8, Dy_2moshi_8 and Tb_2mshi_8 MCs were solved and refined with the Bruker SHELXTL (version 2018/3) software package.[57] All non-hydrogen atoms were refined anisotropically with the hydrogen atoms placed in idealized positions. The SQUEEZE subroutine of the PLATON[58,59] program suite was used in each case to address some of the disordered solvent molecules contained in solvent accessible voids present in the structure which are common in this type of macromolecular complex.[60–62] Additional details are presented in **Table S1**, in the Supporting Information, and in CIF files. Crystals of other $Ln_2L'_8$ MCs (L' = shi^{3-}, $moshi^{3-}$, $mshi^{3-}$) were screened to determine unit cell parameters (**Table S2**).

Powder X-ray diffraction (PXRD) patterns were acquired for $Ln_2L'_8$ MCs using a Rigaku Ultima IV X-Ray Diffractometer (Cu anode, λ = 1.5406 Å) upon scanning from 3 to 15° in 2 θ (**Figure S1**, Supporting Information).

Thermogravimetric analysis curves for Tb_2mshi_8, Tb_2moshi_8, and Tb_2nha_8 were measured from 30 °C to 900 °C under a N_2 atmosphere using a Perkin-Elmer TGA-7 thermogravimetric analyzer at a scan rate of 10 °C/minute (**Figure S12**). Initial sample masses were between 2.5 and 4.9 mg.

Photophysical properties.

Excitation and emission spectra, luminescence lifetimes, and quantum yields. Luminescence data were collected for relevant Tb^{3+} and Sm^{3+} samples in the solid state. Emission and excitation spectra were measured on a Horiba-Jobin-Yvon Fluorolog 3 spectrofluorimeter using a visible photomultiplier tube (PMT) (220–800 nm, R928P; Hamamatsu). All spectra were corrected for the instrumental functions. Luminescence lifetimes were determined under excitation at 355 nm provided by a Nd:YAG laser (YG 980; Quantel), the signals of Tb^{3+} at 545 nm ($^5D_4 \rightarrow {}^7F_5$ transition) or Sm^{3+} at 597 nm ($^4G_{5/2} \rightarrow {}^6H_{7/2}$ transition) were detected with a Hamamatsu R928 PMT connected to an iHR320 monochromator (Horiba Scientific). No initial delay was applied and luminescence decay curves were recorded with time intervals of 0.1/0.2 μs for Tb^{3+} MCs or 20 ns for Sm^{3+} MCs. Representative luminescence decay curves are given in **Figure S13**. The output signals from the detectors were fed into a 500 MHz bandpass digital oscilloscope (TDS 754C; Tektronix). Luminescence lifetimes are averages of at least three independent measurements. Ln^{3+}-centered quantum yields under ligands excitation ($Q_{\mathrm{Ln}}^{\mathrm{L}}$) were determined with a Fluorolog 3 spectrofluorimeter based on the absolute method using an integration sphere (Model G8, GMP SA, Renens, Switzerland). Each sample was measured several times. The experimental error for the determination of quantum yields is estimated as ~10 %. Ligand-centered quantum yields ($Q_{\mathrm{L}}^{\mathrm{L}}$) were calculated from the corresponding emission spectra taking into account the values of $Q_{\mathrm{Ln}}^{\mathrm{L}}$.

Diffuse reflectance spectra. For the collection of diffuse reflectance spectra, $Ln_2L'_8$ MCs (5 wt.%) were thoroughly grounded and dispersed in MgO. Measurements were performed on a Jasco V670 UV-visible spectrophotometer in reflectance (R) mode using a horizontal integration sphere accessory at room temperature. To reflect absorbance, diffuse reflectance spectra are presented as Kubelka-Munk function ($(1-R)^2/2R$) vs. wavelength (**Figures 3, S14, S15** Supporting Information).

Phosphorescence spectra. Phosphorescence spectra of Gd^{3+} compounds were measured on powder samples at 77 K on a Horiba-Jobin-Yvon Fluorolog 3 spectrofluorimeter in time-resolved mode.

Temperature-dependent emission spectra. For measurements ca. 50 mg of relevant Tb^{3+} or Sm^{3+} powder samples were pressed into a pellet using a hand pellet press. These were affixed to a copper plate attached to a temperature controller via vacuum grease. The temperature dependent emission spectra were recorded on a double grating excitation spectrofluorimeter equipped with a TRIAX 320 emission monochromator (Fluorolog-3, Horiba Scientific) coupled to a R928 Hamamatsu photomultiplier in a front face acquisition mode. The excitation source was a 450 W Xe arc lamp. Emission spectra were corrected for the detection and optical spectral response of the spectrofluorimeter. The temperature was controlled by a helium closed cycle cryostat with a vacuum system measuring ca. 5×10^{-6} mbar and a Lakeshore 330 temperature controller with a resistance heater. The temperature was adjusted to various settings using the auto-tuning temperature controller from ca. 11 to 400 K with a maximum accuracy of 0.1 K. Emission spectra were collected after waiting for a minimum of 5 minutes to thermalize the sample. A baseline correction was performed on each spectrum by fitting a polynomial function to the background signal and subtracting the fitted function.

RESULTS

Twelve metallacrown complexes were analyzed for their relevant luminescence properties. Each of these compounds are dimeric 12-MC-4 MCs with a similar topology to that shown in **Figure 1**. The MC units (**Figure 2**, left) form the dimer when combined with the iph^{2-} ligand (**Figure 2**, right). These materials were created using permutations of several different trivalent lanthanide ions (Ln^{3+}) and four MC component ligands (**Figure 2**, center): H_3shi, 5-methylsalicylhydroxamic acid H_3mshi, 5-methoxysalicylhydroxamic acid H_3moshi, and 3-hydroxy-2-naphthohydroxamic acid H_3nha. Each complex has the general formula $Ln_2Ga_8L'_8L''_4$, where Ln = Gd^{3+}, Tb^{3+}, or Sm^{3+}; L' = shi^{3-}, $mshi^{3-}$, $moshi^{3-}$, or nha^{3-}; and L" = iph^{2-}. The complexes will be referred to in shorthand here as $Ln_2L'_8$ for simplicity (e.g., Sm_2shi_8). The Ln_2shi_8 MCs were previously reported for their room temperature luminescence properties[53] (several previously reported data are provided in this work for comparison with the novel complexes). A new analysis of their thermal-dependence of luminescence spectra has been performed. The Ln_2mshi_8, Ln_2moshi_8, and Ln_2nha_8 are all new complexes on which a similar analysis has been performed. Compositions of these complexes have been confirmed by mass spectrometry, elemental analysis, and either single crystal X-ray diffraction or PXRD studies.

For the Tb^{3+} and Sm^{3+} complexes, measured photophysical properties include diffuse reflectance spectra, excitation spectra, emission spectra (11–400 K), emission lifetimes and quantum yields, at room temperature. Emission properties were determined upon excitation into ligand electronic levels in the UV/visible range. Gd^{3+} complexes were synthesized to serve as probes of the ligand-centered electronic structure and were analyzed by recording diffuse reflectance spectra to determine the ligand singlet state energies and phosphorescence spectra to determine the ligand triplet state energies. Such measurement is possible because Gd^{3+} possesses excited electronic states generally too high in energy to accept energy from the ligand excited states, and also because Gd^{3+} possesses very high spin (ground S=7/2) that may increase the rate of singlet to triplet intersystem crossing within the ligand.

Synthesis. The reaction between $Ga(NO_3)_3$, $Ln(NO_3)_3$, isophthalic acid, and the MC ring ligand (H_3shi, H_3mshi, H_3moshi, or H_3nha) in an appropriate ratio of DMF with a basic salt (NH_4HCO_3 for Ln_2shi_8 compounds or NaOH for the others) results in the formation of the desired compounds via self-assembly. These are crystallized out of solution via slow evaporation of the solvent to yield the pure materials.

Crystal Structures. X-ray single crystal structures were solved for at least one Ln^{3+} derivative from each $Ln_2L'_8$ series, e.g. for Tb_2mshi_8, Dy_2moshi_8, and Sm_2nha_8. For Ln_2shi_8, the crystal structure of the Dy^{3+} analogue was previously reported.[51] For the remaining $Ln_2L'_8$ MCs (L' = shi^{3-}, $moshi^{3-}$, $mshi^{3-}$), their unit cells were determined by screening single crystals by X-ray diffraction (**Table S2**). For the $Ln_2L'_8$, only the Sm^{3+} analogue produced crystals suitable for single crystal X-ray diffraction. Tb_2nha_8 and Gd_2nha_8 MCs were obtained as microcrystalline materials. To confirm the structural uniformity within the Ln_2nha_8 series, the corresponding PXRD patterns were acquired and compared with those calculated from the respective crystal structures (**Figure S1**). The collected data allowed to establish a global description of the MC structure for each series, independently of the nature of Ln^{3+}.

The crystal structures of $Ln_2L'_8$ and packing diagrams are shown in **Figures S2-S10**. Each compound has a similar overall topology dictated by the identical ligand binding motifs, resulting in dimeric structures like the one presented in **Figure 1**. The isostructural nature of these complexes indicates that differences in the energy levels of the lanthanides due to crystal field effects will be minimal and that most of the relevant differences in properties are due to the interaction of the Ln^{3+} excited states with the ligand excited states. According to a SHAPE analysis, the local environment around each Ln^{3+} is best described as a square antiprism that is constituted of eight oxygen atoms (**Tables S5-S18**).[63,64] Four of these atoms are carboxylate oxygens derived from isophthalate groups, while the other four oxygen donors are oxime oxygens located in the MC plane. In each case, the isophthalic acid mean plane is closer to the Ln^{3+} than the oxime oxygen plane, ca. 1.1 Å versus 1.5 Å, respectively (**Table S3**). The intramolecular Ln^{3+}–Ln^{3+} distance varies between 7.010–7.215 Å, while the shortest intermolecular distance between Ln^{3+} is at least 12.8 Å (**Table S4**).

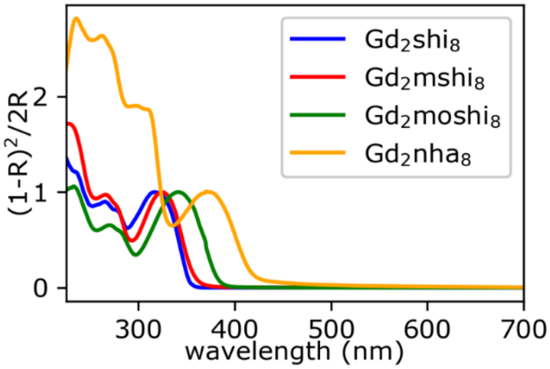

Figure 3. Diffuse reflectance spectra of Gd$_2$L'$_8$ MCs (L' = shi^{3-}, moshi^{3-}, mshi^{3-}, nha^{3-}) presented as Kubelka–Munk function *vs.* wavelength. Spectra are normalized to the lowest energy peak in the spectral range of 290–425 nm.

Thermogravimetric analysis. *Thermogravimetric* curves for Ln$_2$L'$_8$ MCs (L' = shi^{3-}, moshi^{3-}, mshi^{3-}, nha^{3-}) are presented in **Figure S12.** Water and DMF are co-crystallized with the present compounds. All samples show gradual or step-wise weight loss from 30 °C to 200–300 °C associated with the baking of solvent molecules from the lattice, followed by a leveling off until 400–500 °C. Finally, the molecular thermal decomposition occurs above this temperature. These results suggest that MC scaffolds are thermally stable until at least 400 °C (673 K).

Diffuse reflectance spectra. The diffuse reflectance spectra were collected for all studied MCs (**Figure S14**, **S15**, Supporting Information), the spectra corresponding to the Gd^{3+} derivatives are given in **Figure 3**. For each L' ligand, the spectra are quite similar for all three examined Ln^{3+}, so we will focus on Gd^{3+} MCs. We consider the red edge of the spectrum as the singlet state of lowest energy (S$_1$). The singlet energies determined in this manner for each compound are gathered in **Table 2**.

Phosphorescence spectra of Gd^{3+} complexes. Phosphorescence spectra were collected for each Gd^{3+} derivative at 77 K upon excitation into the ligand absorption band between 310–400 nm. The spectra are given in **Figure S16**. Each phosphorescence spectrum was fitted as a sum of Gaussian curves. The lowest in energy Gaussian band was considered as the zero-phonon (0–0) transition was assigned as the energy of the triplet state of lowest energy (T$_1$). These results are gathered in **Table 2**.

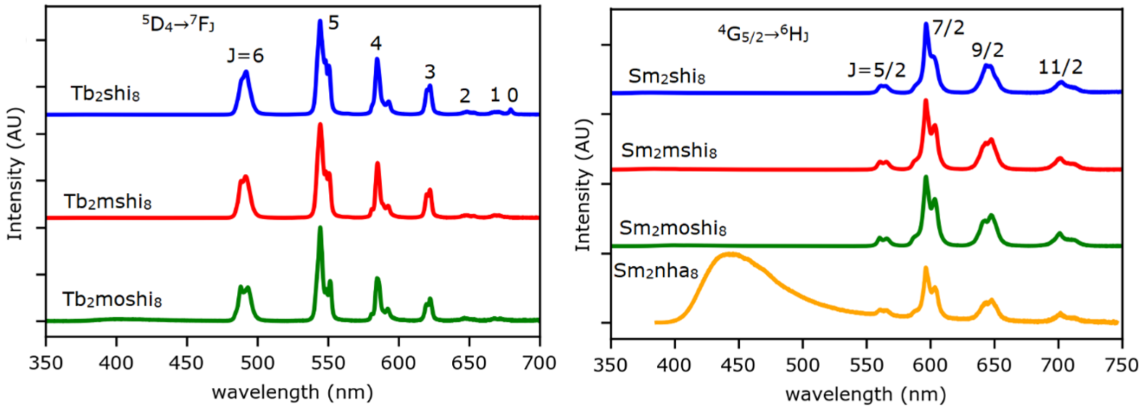

Figure 4. Corrected and normalized emission spectra for Tb$_2$L'$_8$ and Sm$_2$L'$_8$ MCs (L' = shi^{3-}, moshi^{3-}, mshi^{3-}, nha^{3-}) in the solid state upon excitation at 340–370 nm at room-temperature.

Excitation and emission spectra measured at room temperature. Excitation and emission spectra of Tb$_2$L'$_8$ and Sm$_2$L'$_8$ MCs were recorded in the solid state at room temperature. Excitation spectra upon monitoring emission of Tb^{3+} at 545 nm ($^5D_4 \rightarrow {}^7F_5$ transition) and Sm^{3+} at 597 nm ($^4G_{5/2} \rightarrow {}^6H_{7/2}$ transition) are given in **Figures S17** and **S18 (left)**, respectively. Emission spectra upon excitation at

340–370 nm are given in **Figure 4**. Notably, Tb^{3+}-centered emission in Tb_2nha_8 was not observed, while for Sm_2nha_8 a broad band in the range 400–600 nm attributed to the ligand fluorescence was detected along with weak sharp Sm^{3+}-centered bands. Emission profiles of $Tb_2L'_8$ and $Sm_2L'_8$ MCs are independent of the nature of the ligands, being consistent with the locally isostructural coordination environment around each Ln^{3+}. $Tb_2L'_8$ MCs show characteristic emission bands arising from $^5D_4\rightarrow{}^7F_J$ transitions, with the main emission bands attributed to $^5D_4\rightarrow{}^7F_6$ (490 nm), $^5D_4\rightarrow{}^7F_5$ (545 nm), $^5D_4\rightarrow{}^7F_4$ (585 nm), $^5D_4\rightarrow{}^7F_3$ (620 nm), and emission bands with lower intensities assigned to $^5D_4\rightarrow{}^7F_2$ (650 nm), $^5D_4\rightarrow{}^7F_1$ (670 nm), and $^5D_4\rightarrow{}^7F_0$ (680 nm). $Sm_2L'_8$ MCs demonstrate characteristic emission signals arising from $^4G_{5/2}\rightarrow{}^6H_J$ transitions, with bands located at $^4G_{5/2}\rightarrow{}^6H_{5/2}$ (555 nm), $^4G_{5/2}\rightarrow{}^6H_{7/2}$ (600 nm), $^4G_{5/2}\rightarrow{}^6H_{9/2}$ (645 nm), and $^4G_{5/2}\rightarrow{}^6H_{11/2}$ (700 nm). For the Sm_2shi_8, Sm_2mshi_8, and Sm_2moshi_8 compounds, emission in the near infrared (NIR) range was also observed (**Figure S18, right**).

Table 1. Luminescence lifetimes (τ_{obs}), Ln^{3+}-centered quantum yields (Q^{L}_{Ln}) and ligand-centered quantum yields (Q^{L}_{L}) in the visible range of $Tb_2L'_8$ and $Sm_2L'_8$ MCs (L' = shi^{3-}, $moshi^{3-}$, $mshi^{3-}$, nha^{3-}) in the solid state.[a]

MC	τ_{obs} (μs)[b]	Q^{L}_{Ln} (%)	Q^{L}_{L} (%)[c]
Tb_2shi_8	1410(1)[d]	31.2(2) [d,e]	0.105(1)
Tb_2mshi_8	869(2): 92.2(8)% 217(3): 7.8(8) %	25.2(4) [e]	0.106(1)
Tb_2moshi_8	71.6(9): 74.0(5)% 16.1(6): 26.0(5)%	2.07(6) [e]	0.11(1)
Sm_2shi_8	117(1)[d]	2.09(5) [d,e]	0.038(1)
Sm_2mshi_8	76(1)	2.21(2) [e]	0.068(1)
Sm_2moshi_8	83(3)	2.27(5) [e]	0.07(1)
Sm_2nha_8	-[f]	0.0267(7) [g]	0.152(4)

[a] At room temperature, 2σ values between parentheses. Estimated experimental errors: τ_{obs}, ±2%; Q^{L}_{Ln} , ±10 %; Q^{L}_{L} , ±10 %. [b] Under excitation at 355 nm. If a biexponential decay was observed, population parameters $P_i = \frac{B_i\tau_i}{\sum_{i=1}^{n} B_i\tau_i}$ in % are given after the colon. [c] Calculated from the emission spectrum [d] From Ref.[53] [e] Under excitation at 350 nm. [f] Could not be determined due to insufficient signal. [g] Under excitation at 370 nm.

Quantum yields and Ln^{3+} luminescence lifetimes at room temperature. Quantum yields under ligand excitation of (i) Ln^{3+}-centered emission (Q^{L}_{Ln}) and (ii) ligand-centered emission (Q^{L}_{L}) were determined for Ln_2mshi_8, Ln_2moshi_8, and Ln_2nha_8 (Ln = Tb^{3+}, Sm^{3+}) in the solid state. Additionally, Ln^{3+} luminescence lifetimes (τ_{obs}) were determined for all studied MCs except Sm_2nha_8, which exhibited a very weak emission. These parameters are gathered for visible emissions in **Table 1**. Quantum yields for near infrared emission from Sm^{3+} compounds are given in **Table S19**.

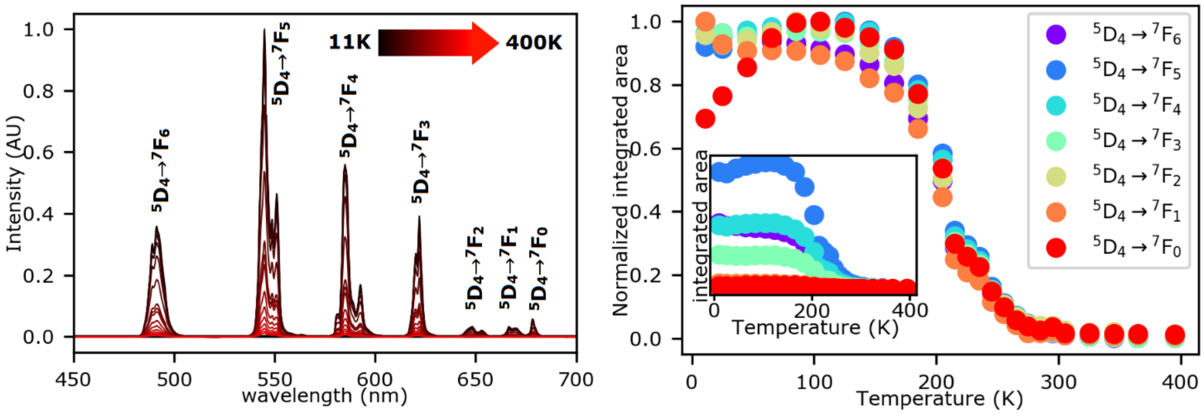

Figure 5. Left: thermal dependence of emission spectrum for Tb_2moshi_8 from 11K (black) to 400K (red) under excitation at 370 nm. Several temperature traces are omitted for clarity. Right: Normalized integrated intensities of each transition *vs*. temperature. The inset shows the non-normalized basis. See **Figure S21** for integration bounds.

Thermal dependence of Ln^{3+}emission intensities. For all MCs exhibiting Tb^{3+}- or Sm^{3+}-centered transitions, emission spectra were collected in the temperature range from 11 to 400 K on solid-state samples. As an example, the thermal dependence of the Tb^{3+} emission in Tb_2moshi_8 is given in **Figure 5** (left). The emission intensity of each band decreases upon heating. In **Figure 5** (right), the normalized integrated intensity of each $^5D_4 \rightarrow ^7F_J$ transition band as a function of temperature is given. All bands possess identical thermal dependence when normalized.

The thermal dependence was analyzed in a similar way for all complexes; those data are summarized in **Figures S19-S25**. The analysis of the thermal dependence of integrated intensities of a representative prominent band for $Tb_2L'_8$ and $Sm_2L'_8$ MCs is given in **Figure 6**. A plot displaying the temperature-dependent emission spectra focusing on the $^5D_4 \rightarrow ^7F_5$ transition for Tb^{3+} complexes and the $^4G_{5/2} \rightarrow ^6H_{7/2}$ transition for Sm^{3+} complexes is given in **Figure S27**.

Analysis of a molecular thermometer based on mixed Tb_2moshi_8/Sm_2moshi_8. The Tb_2moshi_8 and Sm_2moshi_8 complexes were combined to create a ratiometric luminescent nanothermometer. This was accomplished by a thorough grinding of Tb_2moshi_8 and Sm_2moshi_8 in a 1:1 ratio in a mortar. The thermal-dependent luminescence was examined upon excitation at 370 nm (**Figure 7 A**). We observe some overlap between the Sm^{3+} and Tb^{3+} emission profiles, particularly between the Tb^{3+} $^5D_4 \rightarrow ^7F_4/^4G_{5/2} \rightarrow ^6H_{7/2}$ and the $^5D_4 \rightarrow ^7F_2/^4G_{5/2} \rightarrow ^6H_{9/2}$ transitions. In **Figure 7 C,** several Δ parameters are plotted, where $\Delta = I_{Tb}/I_{Sm}$. Here, I_{Tb} and I_{Sm} are the integrated areas of the specified Tb^{3+} emission band (transitions $^5D_4 \rightarrow ^7F_J$, J = 3, 5, 6), and the band corresponding to the $^4G_{5/2} \rightarrow ^6H_{9/2}$ transition of Sm^{3+}, respectively (**Figure 7 B**). The thermal dependence of this parameter was fit to a single-pathway component using Mott-Seitz model: [65]

$$\Delta = \frac{\Delta_o}{1 + a_1 \cdot e^{\frac{-E_1}{k_B T}}} \qquad \textbf{eqn 1}$$

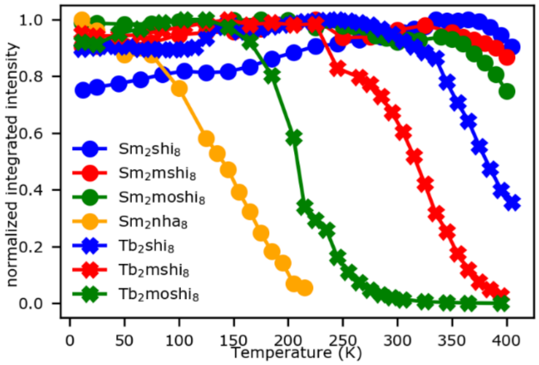

Figure 6. Integrated emission intensities of $^5D_4 \rightarrow ^7F_5$ and $^4G_{5/2} \rightarrow ^6H_{7/2}$ transitions *vs*. temperature for $Tb_2L'_8$ and $Sm_2L'_8$ MCs (L' = shi^{3-}, $moshi^{3-}$, $mshi^{3-}$, nha^{3-}), respectively. For Sm_2nha_8, data are not given above 215 K due to the difficulty in obtaining a signal above the baseline beyond this temperature (see **Figures S25** and **S26**). The excitation wavelength was 340 nm for Ln_2shi_8, 350 nm for Ln_2mshi_8, 370 nm for Ln_2moshi_8, and 380 nm for Ln_2nha_8.

where T is the temperature, a_1 is a dimensionless scaling factor, E_1 is the energy gap between the accepting and donating energy levels, and Δ_o is the maximum intensity of this parameter at low temperatures (before the thermally-dependent quenching pathway activates). The fitting parameters are gathered in **Table S22.** An analogous dual-pathway component Mott-Seitz model can be fit as well (**eqn S1, Table S23**) with similar results. A full theoretical consideration may incorporate many relevant de-activation pathways (*vide infra*) but this simpler model fit the thermal response well in this case. Lastly, **Figure 7 D** shows the relative (thermal) sensitivity of this thermometer (S_r) calculated according to

$$S_r = \frac{1}{\Delta}\left|\frac{\partial \Delta}{\partial T}\right| \qquad \textbf{eqn 2}$$

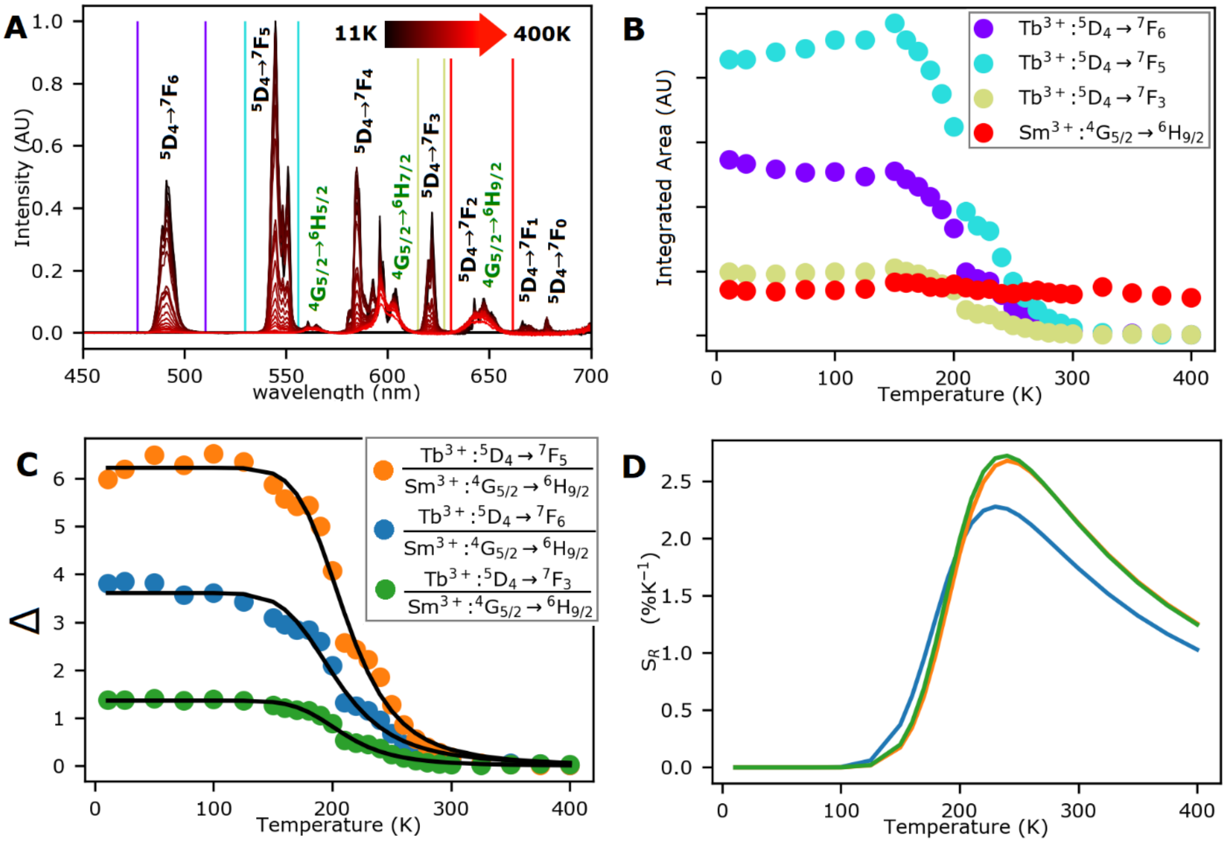

Figure 7. A: thermal dependence of emission spectra for a 1:1 molar mixture of Tb_2moshi_8 and Sm_2moshi_8 from 11 (black) to 400 K (red) under excitation at 370 nm. The Tb^{3+} transitions are identified in black text and the Sm^{3+} ones in green. B: integrated intensities of Tb^{3+} and Sm^{3+} transitions vs. temperature. The integration boundaries are indicated in panel A. For the red integration area, the label "$Sm^{3+}:{}^4G_{5/2}\rightarrow{}^6H_{9/2}$" is indicated because the emission intensity in this spectral region is mainly due to this band, however, the low-intensity "$Tb^{3+}:{}^5D_4\rightarrow{}^7F_2$" transition also occurs within this region. C. The Δ parameter is calculated by taking the fraction specified in the legend for each temperature. The fit for each curve is overlaid in black (**eqn 1**). D: The relative sensitivity for each Δ parameter calculated from **eqn 2**.

DISCUSSION

Emission spectra and quantum yields. The emission spectra of $Tb_2L'_8$ and $Sm_2L'_8$ MCs are quite similar and independent of the nature of the hydroximate ligands. This result can be understood by the locally isostructural environment around each Ln^{3+} center. A C_{4v}-type geometry exists around each Ln^{3+} in $Ln_2L'_8$ MCs, although it is crystallographically C_{4v} for the Ln_2nha_8 and Ln_2mshi_8 compounds and only pseudo-C_{4v} for the Ln_2moshi_8 and Ln_2shi_8 compounds. The small differences in the coordination environment around each Ln^{3+} ion due to the electronic properties of the ligands are apparently minimally important in shaping the emission spectra of each $Ln_2L'_8$ MCs.

A correlation can be established between the photophysical properties of $Ln_2L'_8$ MCs and the relative positions of the levels of the ligands (S_1, T_1) in respect to the accepting levels of the corresponding Ln^{3+}, i.e. $^5D_4$ (20400 cm^{-1}) for Tb^{3+} and $^4G_{5/2}$ (17800 cm^{-1}) for Sm^{3+}. Those data are summarized in **Table 2.** For the Tb_2nha_8 complex, an absence of Tb^{3+}-

centered emission is expected considering that the donating T_1 state of nha^{3-} ligand lies below the $^5D_4$ state of Tb^{3+}. When the $^5D_4$ state is occupied, there is a very efficient deactivation route via energy transfer to the lower-lying T_1 state and/or the sensitization of the Tb^{3+} via the feeding from the T_1 state cannot occur given the lower energy position of the T_1 state.

Table 2. Ligand-centered S_1 and T_1 energy levels, the lowest emitting levels of Sm^{3+} ($^4G_{5/2}$) and Tb^{3+} ($^5D_4$), and relevant energy gaps.

Energy (cm^{-1})	**Ln$_2$shi$_8$**	**Ln$_2$mshi$_8$**	**Ln$_2$moshi$_8$**	**Ln$_2$nha$_8$**
S_1	27800	26900	25400	23300
T_1	21980	21570	21640	18150
$\Delta E(S_1\text{-}T_1)$	5820	5330	3760	5150
$\Delta E(S_1\text{-}^4G_{5/2}{}^a)$	10000	9100	7600	5500
$\Delta E(T_1\text{-}^4G_{5/2}{}^a)$	4180	3770	3840	350
$\Delta E(S_1\text{-}^5D_4{}^b)$	7400	6500	5000	2900
$\Delta E(T_1\text{-}^5D_4{}^b)$	1580	1170	1240	-2250

^{a}17800 cm^{-1}.[66] ^{b} 20400 cm^{-1}.[66]

Among Sm$_2$L'$_8$ MCs, Sm$_2$nha$_8$ exhibits the lowest Q_{Sm}^L (Table 1) and the visible emission spectrum shows significant broad ligand-centered bands compared to the Sm^{3+}-centered transitions (**Figure 4**). The very low quantum yield value recorded for Sm^{3+} in Sm$_2$nha$_8$ can be understood by the small energy gap (ΔE = 350 cm^{-1}) between the $^4G_{5/2}$ state of Sm^{3+} and the T_1 state of the nha^{3-} ligand, enhancing the probability of a back energy transfer. For other studied Sm$_2$L'$_8$ MCs, the energy differences between the corresponding T_1 levels and the $^4G_{5/2}$ state are more than 3770 cm^{-1} and they exhibit very similar values of Q_{Sm}^L (2.0–2.3 %).

In the case of Tb$_2$L'$_8$ MCs (L' = shi^{3-}, moshi^{3-}, mshi^{3-}), the variability of Q_{Tb}^L is larger, ranging from 2.07(6) to 31.2(2) % (Table 1), owing to the closer proximity between the ligand energy levels and the emissive $^5D_4$ energy level of Tb^{3+}. In general, the values of Q_{Tb}^L correlate directly with the energy gap between the donating T_1 and accepting $^5D_4$ levels. That is, the smaller the energy gap $\Delta E(T_1\text{–}\,^5D_4)$, the smaller the room temperature Q_{Tb}^L due mainly to the higher probability of back-energy transfer to the energy states of the ligand. We can note, however, that while Tb$_2$mshi$_8$ and Tb$_2$moshi$_8$ possess fairly similar T_1 energy levels (21570 cm^{-1} and 21640 cm^{-1}, respectively), the Q_{Tb}^L values are significantly different, 25.2(4) % for Tb$_2$mshi$_8$ vs. 2.07(6) % for Tb$_2$moshi$_8$. Thus, we can conclude that the energy transfer involving the S_1 state is also important, since the S_1 energy levels are more disparate (26900 cm^{-1} for Tb$_2$mshi$_8$ vs. 25400 cm^{-1} for Tb$_2$moshi$_8$). This conclusion will be described in more detail below.

Thermal dependence of emission. The luminescence spectra of Ln$_2$L'$_8$ MCs were recorded in a broad range of temperatures from 11 to 400 K. As temperature increases, most of the compounds show an emission intensity that is generally minimally affected until a certain temperature is reached, where a significant thermally activated decrease occurs, consistent with the Boltzmann-dependent nonradiative de-activation mechanism.

Considering the Sm^{3+} compounds, the onset of intensity decrease occurs at low temperatures for Sm$_2$nha$_8$, and at temperatures greater than ~350 K for the other Sm^{3+} MCs. For Sm$_2$nha$_8$, a significant decrease starts around 75 K, although it is not fully apparent from the collected data that the temperature change was flat below to this temperature, as the lowest available temperature point is 11 K. The low temperature onset of this decrease can be understood from the small energy gap (ΔE = 350 cm^{-1}) between the donating T_1 state of the ligand and the accepting $^4G_{5/2}$ state of Sm^{3+}. This small gap indicates that the Boltzmann-dependent back energy transfer will occur at low temperatures. For the other Sm^{3+} MCs, their intensity decrease trend is not complete within the experimental temperature range. However, each compound initiates a temperature decrease around 350 K. The similarity of the temperature decrease onset for each of these MCs, despite a variety of ligand energy levels, suggests that the intensity decrease in these cases may be primarily due to mechanisms that may be additional to the electronic-based energy transfer. Thermally activated vibrational modes may be the most relevant non-radiative deactivation mechanisms owing to the similarity of the molecular structure within Sm$_2$L'$_8$ series. Thermally activated solvent loss may also be relevant at high temperatures (see TGA, **Figure S12**).

For the Tb^{3+} complexes, the variation in thermally dependent emission intensity behaviors as related to the energy levels of the ligand states is more apparent than for the Sm^{3+} complexes. The intensity decrease begins around 150 K for Tb$_2$moshi$_8$, 250 K for Tb$_2$mshi$_8$, and 300 K for Tb$_2$shi$_8$. This trend correlates well with the energy gap between the ligand-based energy levels and the $^5D_4$ state of

Tb^{3+} in each case. For the S_1 energy level of the ligand: $shi^{3-} > mshi^{3-} > moshi^{3-}$. For the T_1 energy level: $shi^{3-} > mshi^{3-} \approx moshi^{3-}$. Thus, given the differences in Q_{Tb}^{L} values discussed above, energy transfer dynamics considering the S_1 as well as the T_1 state are quite relevant. Otherwise, only the T_1 states would be important and the Tb_2moshi_8 and Tb_2mshi_8 MCs would have similar thermal responses and Q_{Tb}^{L} at room temperature since the T_1 energy levels are similar for Tb_2moshi_8 and Tb_2mshi_8 MCs.

To examine the importance of the relative energy levels in each emissive compound in detail, theoretical calculations were performed. The thermal response of each material was calculated considering Judd–Ofelt theory, intramolecular energy transfer (IET) theory, and population rate equations.[67]

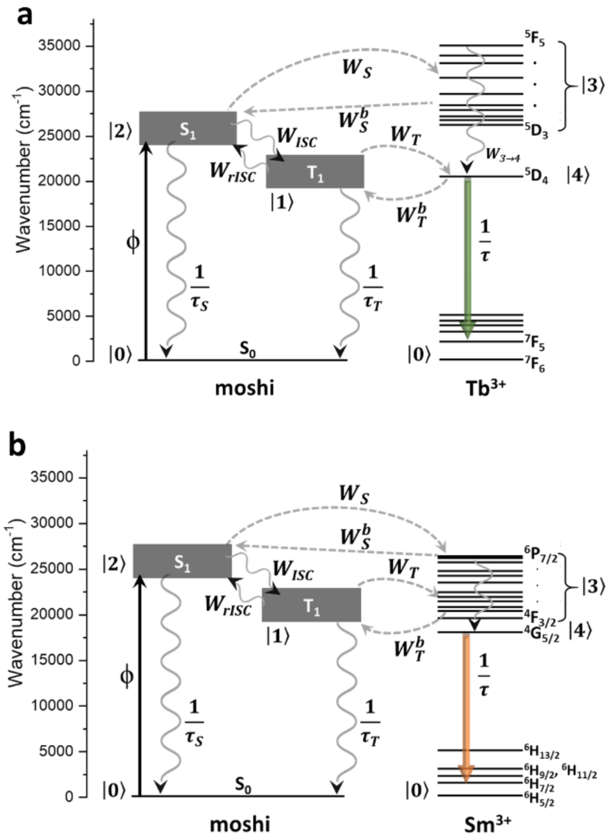

Figure 8. Simplified energy level diagrams for Ln_2moshi_8. **a)** Ln = Tb^{3+} and **b)** Ln = Sm^{3+}. ϕ is the rate of population of the singlet state upon absorption of the excitation light ($S_0 \rightarrow S_1$), W_{ISC} is the $S_1 \rightarrow T_1$ intersystem crossing rate while W_{rISC} is the rate of the reverse process ($T_1 \rightarrow S_1$). W_S and W_T are the forward IET rates from the S_1 and T_1 states, respectively. Their backward IET rates are the ones with the superscript b (W^b). $W_{3\rightarrow4}$ is the decay rate from Ln^{3+} upper levels to the emitting one, $|3\rangle \rightarrow |4\rangle$. The luminescence lifetimes τ_S, τ_T, and τ are related to the S_1, T_1, and Ln^{3+} states, respectively.

The full theoretical analysis can be found in the Supporting Information; however, a summary of the results is given here (**Figure 8**). For most of the Tb^{3+}-based MCs, the temperature-dependent behavior can be understood as a competition between forward and backward rates via energy transfer involving the S_1 state (W_S and W_S^b, **Table S35**). On the other hand, for the Sm^{3+}-based MCs, the energy transfer from the T_1 state was shown to be more efficient and the forward rate ($W_T \sim 10^9\ s^{-1}$) increases with the temperature for all cases. **Figure S33** summarizes the thermal behavior of some important rates.

Among all of the studied MCs, the Ln_2moshi_8 is a special case in which the energy transfer dynamics between the T_1 and S_1 states of the $moshi^{3-}$ ligand are especially important. This observation is based on the close energetic proximity of these electronic states $\Delta E(S_1\text{–}T_1)$ = 3760 cm^{-1}, promoting a reverse intersystem crossing rate $T_1 \rightarrow S_1$ (W_{rISC}).[68,69] Thus, the W_{rISC} becomes commensurate with the direct process (W_{ISC}) and imposes a thermally dependent rate competition between them (**Figure S34**). In other words, as the temperature increases, W_{rISC} becomes competitive with W_{ISC}, so the T_1 state becomes less populated and can no longer transfer as much energy to the Tb^{3+}, decreasing the population of the $^5D_4$ level (**Figure S35**). If the effect of W_{rISC} is not considered, only the backward energy transfer via S_1 (W_S^b) is sensitive to the temperature (W_S^b ranging from 1.15×10^5 to 1.81×10^6 s^{-1}), which is not substantial enough to produce the rapid Tb^{3+} emission quenching pattern observed experimentally when the temperature raises for Tb_2moshi_8 (**Figure S28**). On the other hand, the competition between W_{ISC} and W_{rISC} does not affect too much the Sm_2moshi_8 once the rates $T_1 \rightleftarrows Sm^{3+}$ (W_T and W_T^b, **Table S35**) are faster than the estimated W_{ISC} and W_{rISC} (**Figure S34**).

Therefore, the energy transfer in both directions across the S_1–T_1 energy gap is a highly important mechanism for the induction of a thermal dependence of the emission intensity in competition with the Ln^{3+} to T_1 mechanism which has been previously identified.[36,45,48,50] Based on these results, one may consider adjusting the ligand S_1–T_1 gap to induce changes in the thermal dependence of thermometer, or to increase quantum yields of emission. In the present case, this process does not greatly affect the Sm_2moshi_8 because it holds the $W_T > W_{rISC}$ relation for any temperature considered. The W_{rISC} is negligible for each of the other ligands due to high $\Delta E(S_1\text{–}T_1)$ (> 5000 cm^{-1}).

It is important to keep in mind that large forward rates (from ligand to the Ln^{3+}) will not grant necessarily to the system excellent optical properties, and that the entire set of competing rates are difficult to generalize heuristically. This set can only be examined with the help of population rate equations (**eqns. S20–S24**) that take into account all rates involved (absorption, ISC, rISC, forward IET, backward IET, and luminescence decay lifetimes), as depicted in **Figure 8**.

Knowing the thermal behavior of the population of the emitting level for both Tb^{3+} and Sm^{3+} (**Table S36**), it is possible to model the Δ parameters. **Figure 9** shows the theoretical curves for a 1:1 mixture of Tb_2moshi_8:Sm_2moshi_8. It is notable the similarity between the theoretical Δ with the experimental ones (**Figure 7C**). The separations between the three curves are related to the differences in the radiative components for each Tb^{3+} $^5D_4 \rightarrow {}^7F_J$ transition (J = 3, 5, and 6). It is worth highlighting that the theoretical modeling procedure presented here is general and capable of estimating the relative population of emitting levels of any Ln^{3+} ion, and therefore, the emission intensity (or ratio between two intensities). This feature opens perspectives in the rational design of new luminescence Ln^{3+}-based materials before realizing synthetic routes.

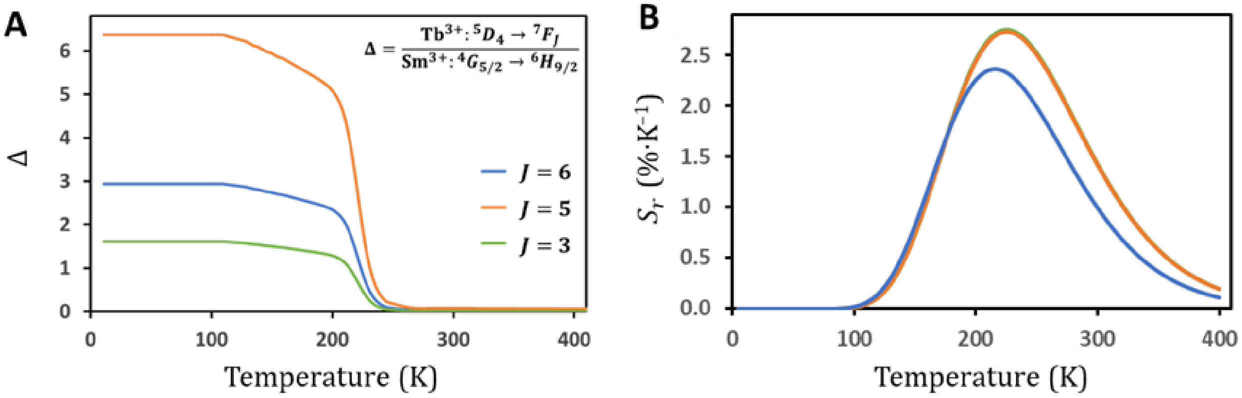

Figure 9. Theoretical thermometric Δ parameters (**A**) and sensitivity (**B**) for 1:1 Tb_2moshi$_8$:Sm_2moshi$_8$. Compare to experimental results (**Figure 7 C, D**).

The comparison between the temperature-dependent emission profiles of the ${}^5D_4 \rightarrow {}^7F_5$ transition for $Tb_2L'_8$ MCs and the ${}^4G_{5/2} \rightarrow {}^6H_{7/2}$ transition for $Sm_2L'_8$ MCs are presented in **Figure S27**. We can observe that the intensity of the Tb^{3+} transition decreases as temperature increases while maintaining an overall similar spectral profile, while for the Sm^{3+} complexes, the profile of the ${}^4G_{5/2} \rightarrow {}^6H_{7/2}$ transition broadens noticeably throughout the experimental temperature range even if the emission intensity is relatively constant. This behavior is consistent with the thermal population and the emission from excited states located lower -lying above the lowest-energy emitting level of Sm^{3+} as temperature increases. For Tb^{3+}, maintaining the same spectral profile suggests that the electronic states above the ${}^5D_4$ emitting level are not populated as temperature increases.

It is worth mentioning that when the S_1 is repopulated by the reverse ISC (rISC) pathway, the competition between $S_1 \rightarrow S_0$ and $S_1 \rightarrow Ln^{3+}$ is considered in the numerical simulations (coupled system of rate equations). The first process prevails over the second one theoretically and experimentally. Otherwise, if $(\tau_S)^{-1} < W_S$, an increase of the Tb^{3+} ${}^5D_4$ population (and consequently Tb^{3+} emission) would be expected with the increase of the rISC when the temperature rises (**Figure S34**).

Analysis of thermometric device capacity. One may notice than any permutation of the present compounds could be used to create a luminescent thermometer provided that one of the emitters (Sm^{3+}, in this case) has a relatively constant response to temperature (to serve as a calibration) and the other (Tb^{3+}) has a decrease in intensity in the region of interest. Thus, because the present set of $Ln_2L'_8$ MCs has a variability in the location of the thermal dependence throughout the cryogenic to 400 K range, these materials represent a way to create luminescent thermometers for use in an arbitrary temperature range.

As an example, a 1:1 mixture of Tb_2moshi$_8$:Sm_2moshi$_8$ was combined in the solid state to demonstrate the thermometric capacity of the present complexes by mixing two independent materials. The thermometric analysis described above **(eqn 2)** led to a luminescent molecular thermometer with a maximal sensitivity S_r around 3 %K^{-1} at 220 K, but S_r > 1.5 %K^{-1} for ca. 200–300 K (**Figure 7**). Since the thermal dependence is controlled mainly by the Tb^{3+}, by using a different Tb^{3+}-based compound, we can access a broad temperature range for thermometric activity. For example, we can expect a S_r that is larger than 1.5 %K^{-1} throughout the biologically relevant range 300–350 K by using Tb_2mshi$_8$ (**Figure S29**). Thermogravimetric analysis of $Ln_2L'_8$ revealed that these dimeric MCs are very robust, being thermally stable up to at least 650 K (**Figure S12**).

When using intensity-based luminescence thermometry, a second emitter is necessary to allow the internal calibration of the thermometric response, as abovementioned. As in the present case, the second ("calibrating") emitter does not need to be covalently attached to the active (thermally responsive) center if these emitters are evenly dispersed within the environment of interest. Although one may think about covalent bonding of the two emissive centers (thermally active and calibrating), this may not necessarily be beneficial versus the simpler approach of using two independent types of molecules. For the presented MCs and many other thermometric systems, Boltzmann dependent energy transfer is the relevant thermally active mechanism.[70] As a statistical process, a Boltzmann dependent mechanism requires an ensemble of emitters to allow the accurate correlation of intensity with the temperature.

Molecular-based thermometers composed of two independently emissive Ln^{3+} are promising because they offer the sensitivity of a dual-centered ratiometric optical nanothermometer: the two emissions used for analysis can be independently modified, and the molecule itself can be functionalized via chemical techniques. For example, in a previous communication, we showed that one may combine 1:1 Sm_2shi$_8$:Tb_2shi$_8$ in polystyrene nanobeads to create a water-compatible compound with thermometric activity in a biologically relevant range, 300–330 K.[71]

CONCLUSIONS

Twelve Ln^{3+}-based metallacrowns (Ln$_2$L'$_8$, L' = shi^{3-}, moshi^{3-}, mshi^{3-}, nha^{3-}) were analyzed for their optical properties, including nine newly synthesized complexes. Three new molecular scaffolds were presented (Ln$_2$moshi$_8$, Ln$_2$mshi$_8$, Ln$_2$nha$_8$), along with a previously described Ln$_2$shi$_8$ MCs. The Gd^{3+}, Sm^{3+}, and Tb^{3+} complexes were presented in each case, and the temperature response of the Ln^{3+}-based photoluminescence was measured for the Sm^{3+} and Tb^{3+} complexes. The analysis of the diffuse reflectance and phosphorescence spectra of the corresponding Gd^{3+} MCs allowed the determination of the ligand S$_1$ and T$_1$ energy levels. It was generally found that the energy gap ΔE between the Ln^{3+} excited state and the ligand excited T$_1$ state is correlated with the temperature of onset of the reduced emission intensity. The smaller ΔE led to a decrease of the emission intensity, which was onset at lower temperatures consistent with a Boltzmann-dependent back transfer mechanism. Furthermore, theoretical calculations allowed the identification of an important T$_1$ to S$_1$ back energy transfer mechanism for thermally-dependent deactivation of the Tb$_2$moshi$_8$ complex. The difference in energies T$_1$–S$_1$ together with Ln^{3+*}–T$_1$ represent an important parameter for creating thermally active luminescent materials. This approach is advantageous because it is based on a purely molecular mechanism, independent of the properties of the bulk material.

It was shown that within the studied series of MCs, a thermal response could be modulated across the cryogenic to 400 K range. In addition, by combining MCs with different thermal dependence, an optical ratiometric thermometer could be produced. Such thermometer functionality was demonstrated with the 1:1 Tb$_2$moshi$_8$:Sm$_2$moshi$_8$ system in the solid state, which had a maximum relative thermal sensitivity S_r of about 3 %K^{-1} at 220 K but S_r > 1.5 %K^{-1} in the range 200–300 K. The presented approach of combining two materials with a disparate thermal response could be generally translated for other classes of compounds to create optical thermometers with controlled properties and improved performance. Due to the tunability of the temperature range via synthetic considerations, physical processes which are active at different thermal ranges can be accessed with the present scheme. For example, a Tb$_2$mshi$_8$-based system can be expected to have a high thermal sensitivity at ca. 300 K (**Figure 6**), i.e. in a biologically relevant range. A combination of this MC with an appropriate partner complex such as Sm$_2$mshi$_8$ could allow to create a ratiometric thermometer.

ASSOCIATED CONTENT

Crystallographic information files (.cif) for Tb$_2$mshi$_8$ (CCDC 2170006), Sm$_2$nha$_8$ (CCDC 2170007), and Dy$_2$moshi$_8$ (CCDC 2170008).

Experimental details, synthesis and characterization of Ln-1 MCs, X-ray crystallographic parameters, supplementary tables, figures describing photophysical properties, and theoretical analysis details are available in supporting information (PDF).

ACKNOWLEDGMENTS

This research was supported in part by the National Science Foundation (NSF) under grants CHE-1664964 (V.L.P.), CHE- 0840456 (X-ray instrumentation), and DGE-1256260 (E.V.S). EVS thanks Rackham Graduate School (University of Michigan) and the Chateaubriand Fellowship of the Office for Science & Technology of the Embassy of France in the United States. This work was developed within the scope of the projects CICECO-Aveiro Institute of Materials, UIDB/50011/2020, UIDP/50011/2020 & LA/P/0006/2020, and The Shape of Water (PTDC/NAN-PRO/3881/2020) financed by national funds through the FCT/MCTES (PIDDAC). The work in France was partially supported by Ligue Régionale Contre le Cancer, comité du Loiret et d'Eure-et-Loir, the network «Molécules marines, métabolisme et cancer» from the Cancéropôle Grand Ouest. S.P. acknowledges support from the Institut National de la Santé et de la Recherche Médicale (INSERM).

ABBREVIATIONS

IET, intramolecular energy transfer; ISC, intersystem crossing; MC, metallacrown; PXRD, powder X-ray diffraction; rISC, reverse intersystem crossing.

REFERENCES

(1) Grodzinsky, E.; Sund Levander, M. History of the Thermometer. In *Understanding Fever and Body Temperature*; Grodzinsky, E., Sund Levander, M., Eds.; Springer International Publishing: Cham, 2020; pp 23–35. https://doi.org/10.1007/978-3-030-21886-7.

(2) Araújo, A. Multi-Spectral Pyrometry—a Review. *Meas. Sci. Technol.* **2017**, *28* (8), 082002. https://doi.org/10.1088/1361-6501/aa7b4b.

(3) Ni, P. A.; More, R. M.; Yoneda, H.; Bieniosek, F. M. Polarization Pyrometry: An Improvement to Multi-Wavelength Optical Pyrometry. *Rev. Sci. Instrum.* **2012**, *83* (12), 1–7. https://doi.org/10.1063/1.4768473.

(4) Quintanilla, M.; Liz-Marzán, L. M. Guiding Rules for Selecting a Nanothermometer. *Nano Today* **2018**, *19*, 126–145. https://doi.org/10.1016/j.nantod.2018.02.012.

(5) Brites, C. D. S.; Lima, P. P.; Silva, N. J. O.; Millán, A.; Amaral, V. S.; Palacio, F.; Carlos, L. D. Organic-Inorganic Eu3+/Tb3+ Codoped Hybrid Films for Temperature Mapping in Integrated Circuits. *Front. Chem.* **2013**, *1* (July), 1–6. https://doi.org/10.3389/fchem.2013.00009.

(6) Okabe, K.; Uchiyama, S. Intracellular Thermometry Uncovers Spontaneous Thermogenesis and Associated Thermal Signaling. *Commun. Biol.* **2021**, *4* (1), 1–7. https://doi.org/10.1038/s42003-021-02908-2.

(7) Piñol, R.; Zeler, J.; Brites, C. D. S.; Gu, Y.; Téllez, P.; Carneiro Neto, A. N.; Da Silva, T. E.; Moreno-Loshuertos, R.; Fernandez-Silva, P.; Gallego, A. I.; Martinez-Lostao, L.; Martínez, A.; Carlos, L. D.; Millán, A. Real-Time Intracellular Temperature Imaging Using Lanthanide-Bearing Polymeric Micelles. *Nano Lett.* **2020**, *20* (9), 6466–6472. https://doi.org/10.1021/acs.nanolett.0c02163.

(8) Ximendes, E.; Marin, R.; Shen, Y.; Ruiz, D.; Gómez-Cerezo, D.; Rodríguez-Sevilla, P.; Lifante, J.; Viveros-Méndez, P. X.; Gámez, F.; García-Soriano, D.; Salas, G.; Zalbidea, C.; Espinosa, A.; Benayas, A.; García-Carrillo, N.; Cussó, L.; Desco, M.; Teran, F. J.; Juárez, B. H.; Jaque, D. Infrared-Emitting Multimodal Nanostructures for Controlled In Vivo Magnetic Hyperthermia. *Adv. Mater.* **2021**, *33* (30), 2100077. https://doi.org/10.1002/adma.202100077.

(9) Graham, E. M.; Iwai, K.; Uchiyama, S.; Prasanna De Silva, A.; Magennis, S. W.; Jones, A. C. Quantitative Mapping of Aqueous Microfluidic Temperature with Sub-Degree

Resolution Using Fluorescence Lifetime Imaging Microscopy. *Lab Chip* **2010**, *10* (10), 1267–1273. https://doi.org/10.1039/b924151e.

(10) Brites, C. D. S.; Millán, A.; Carlos, L. D. Lanthanides in Luminescent Thermometry. In *Handbook on the Physics and Chemistry of Rare Earths*; Bünzli, J.-C. G., Pecharsky, V. K., Eds.; Elsevier: Amsterdam, 2016; Vol. 49, pp 339–427. https://doi.org/10.1016/bs.hpcre.2016.03.005.

(11) Brites, C. D. S.; Balabhadra, S.; Carlos, L. D. Lanthanide-Based Thermometers: At the Cutting-Edge of Luminescence Thermometry. *Adv. Opt. Mater.* **2019**, *7* (5), 1–30. https://doi.org/10.1002/adom.201801239.

(12) Vetrone, F.; Naccache, R.; Zamarrón, A.; De La Fuente, A. J.; Sanz-Rodríguez, F.; Maestro, L. M.; Rodriguez, E. M.; Jaque, D.; Sole, J. G.; Capobianco, J. A. Temperature Sensing Using Fluorescent Nanothermometers. *ACS Nano* **2010**, *4* (6), 3254–3258. https://doi.org/10.1021/nn100244a.

(13) Morinvil, A.; Matulionyte, M.; Cheng, T.; Vetrone, F. Advancing Neodymium Single-Band Nanothermometry. **2019**, *1050* (ii), 11322–11330. https://doi.org/10.1039/c9nr02801c.

(14) Hernández-Rodríguez, M. A.; Lozano-Gorrín, A. D.; Martín, I. R.; Rodríguez-Mendoza, U. R.; Lavín, V. Comparison of the Sensitivity as Optical Temperature Sensor of Nano-Perovskite Doped with Nd3+ Ions in the First and Second Biological Windows. *Sensors Actuators, B Chem.* **2018**, *255*, 970–976. https://doi.org/10.1016/j.snb.2017.08.140.

(15) Quintanilla, M.; Benayas, A.; Naccache, R.; Vetrone, F. Luminescent Nanothermometry with Lanthanide-Doped Nanoparticles. In *Thermometry at the Nanoscale: Techniques and Selected Applications*; Carlos, L. D., Palacio, F., Eds.; Royal Society of Chemistry: Cambridge, 2016; pp 124–166. https://doi.org/10.1039/9781782622031-00124.

(16) Kucsko, G.; Maurer, P. C.; Yao, N. Y.; Kubo, M.; Noh, H. J.; Lo, P. K.; Park, H.; Lukin, M. D. Nanometre-Scale Thermometry in a Living Cell. *Nature* **2013**, *500* (7460), 54–58. https://doi.org/10.1038/nature12373.

(17) Neumann, P.; Jakobi, I.; Dolde, F.; Burk, C.; Reuter, R.; Waldherr, G.; Honert, J.; Wolf, T.; Brunner, A.; Shim, J. H.; Suter, D.; Sumiya, H.; Isoya, J.; Wrachtrup, J. High-Precision Nanoscale Temperature Sensing Using Single Defects in Diamond. *Nano Lett.* **2013**, *13* (6), 2738–2742. https://doi.org/10.1021/nl401216y.

(18) Uchiyama, S.; Gota, C. Luminescent Molecular Thermometers for the Ratiometric Sensing of Intracellular Temperature. *Rev. Anal. Chem.* **2017**, *36* (1). https://doi.org/10.1515/revac-2016-0021.

(19) Arai, S.; Suzuki, M.; Park, S.-J.; Yoo, J. S.; Wang, L.; Kang, N.-Y.; Ha, H.-H.; Chang, Y.-T. Mitochondria-Targeted Fluorescent Thermometer Monitors Intracellular Temperature Gradient. *Chem. Commun.* **2015**, *51*, 8044–8047. https://doi.org/10.1039/c5cc01088h.

(20) Wang, H.; Zhao, D.; Cui, Y.; Yang, Y.; Qian, G. A Eu/Tb-Mixed MOF for Luminescent High-Temperature Sensing. *J. Solid State Chem.* **2017**, *246* (October 2016), 341–345. https://doi.org/10.1016/j.jssc.2016.12.003.

(21) Rocha, J.; Brites, C. D. S.; Carlos, L. D. Lanthanide Organic Framework Luminescent Thermometers. *Chem. - A Eur. J.* **2016**, *22* (42), 14782–14795. https://doi.org/10.1002/chem.201600860.

(22) Bao, G.; Wong, K.-L.; Jin, D.; Tanner, P. A. A Stoichiometric Terbium-Europium Dyad Molecular Thermometer: Energy Transfer Properties. *Light Sci. Appl.* **2018**, *7* (1), 96. https://doi.org/10.1038/s41377-018-0097-7.

(23) Errulat, D.; Marin, R.; Gálico, D. A.; Harriman, K. L. M.; Pialat, A.; Gabidullin, B.; Iikawa, F.; Couto, O. D. D.; Moilanen, J. O.; Hemmer, E.; Sigoli, F. A.; Murugesu, M. A Luminescent Thermometer Exhibiting Slow Relaxation of the Magnetization: Toward Self-Monitored Building Blocks for Next-Generation Optomagnetic Devices. *ACS Cent. Sci.* **2019**, *5* (7), 1187–1198. https://doi.org/10.1021/acscentsci.9b00288.

(24) Brites, C. D. S.; Lima, P. P.; Silva, N. J. O.; Millán, A.; Amaral, V. S.; Palacio, F.; Carlos, L. D. A Luminescent Molecular Thermometer for Long-Term Absolute Temperature Measurements at the Nanoscale. *Adv. Mater.* **2010**, *22* (40), 4499–4504. https://doi.org/10.1002/adma.201001780.

(25) Freddi, S.; Sironi, L.; D'Antuono, R.; Morone, D.; Donà, A.; Cabrini, E.; D'Alfonso, L.; Collini, M.; Pallavicini, P.; Baldi, G.; Maggioni, D.; Chirico, G. A Molecular Thermometer for Nanoparticles for Optical Hyperthermia. *Nano Lett.* **2013**, *13* (5), 2004–2010. https://doi.org/10.1021/nl400129v.

(26) Johansson, M. K.; Cook, R. M.; Xu, J.; Raymond, K. N. Time Gating Improves Sensitivity in Energy Transfer Assays with Terbium Chelate/Dark Quencher Oligonucleotide Probes. *J. Am. Chem. Soc.* **2004**, *126* (50), 16451–16455. https://doi.org/10.1021/ja0452368.

(27) Bünzli, J. G.; Piguet, C. Taking Advantage of Luminescent Lanthanide Ions. *Chem. Soc. Rev.* **2005**, *34*, 1048–1077. https://doi.org/10.1039/b406082m.

(28) Carneiro Neto, A. N.; Mamontova, E.; Botas, A. M. P.; Brites, C. D. S.; Ferreira, R. A. S.; Rouquette, J.; Guari, Y.; Larionova, J.; Long, J.; Carlos, L. D. Rationalizing the Thermal Response of Dual-Center Molecular Thermometers: The Example of an Eu/Tb Coordination Complex. *Adv. Opt. Mater.* **2021**, *2101870*, 1–12. https://doi.org/10.1002/adom.202101870.

(29) Trannoy, V.; Carneiro Neto, A. N.; Brites, C. D. S.; Carlos, L. D.; Serier-Brault, H. Engineering of Mixed Eu 3+ /Tb 3+ Metal-Organic Frameworks Luminescent Thermometers with Tunable Sensitivity. *Adv. Opt. Mater.* **2021**, *9* (6), 2001938. https://doi.org/10.1002/adom.202001938.

(30) Wang, Z.; Ananias, D.; Carné-Sánchez, A.; Brites, C. D. S.; Imaz, I.; Maspoch, D.; Rocha, J.; Carlos, L. D. Lanthanide-Organic Framework Nanothermometers Prepared by Spray-Drying. *Adv. Funct. Mater.* **2015**, *25* (19), 2824–2830. https://doi.org/10.1002/adfm.201500518.

(31) Ren, M.; Brites, C. D. S.; Bao, S. S.; Ferreira, R. A. S.; Zheng, L. M.; Carlos, L. D. A Cryogenic Luminescent Ratiometric Thermometer Based on a Lanthanide Phosphonate Dimer. *J. Mater. Chem. C* **2015**, *3* (33), 8480–8484. https://doi.org/10.1039/c5tc01468a.

(32) Zhao, D.; Zhang, J.; Yue, D.; Lian, X.; Cui, Y.; Yang, Y.; Qian, G. A Highly Sensitive Near-Infrared Luminescent Metal-Organic Framework Thermometer in the Physiological Range. *Chem. Commun.* **2016**, *52* (53), 8259–8262. https://doi.org/10.1039/c6cc02471h.

(33) Xia, C.; Yu, C.; Cao, M.; Xia, J.; Jiang, D.; Zhou, G.; Zhang, D.; Li, H. A Eu and Tb Co-Doped MOF-5 Compound for Ratiometric High Temperature Sensing. *Ceram. Int.* **2018**, *44* (17), 21040–21046. https://doi.org/10.1016/j.ceramint.2018.08.140.

(34) D'Vries, R. F.; Álvarez-García, S.; Snejko, N.; Bausá, L. E.; Gutiérrez-Puebla, E.; de Andrés, A.; Monge, M. Á. Multimetal Rare Earth MOFs for Lighting and Thermometry: Tailoring Color and Optimal Temperature Range through Enhanced Disulfobenzoic Triplet Phosphorescence. *J. Mater. Chem. C* **2013**, *1* (39), 6316. https://doi.org/10.1039/c3tc30858h.

(35) Cui, Y.; Zou, W.; Song, R.; Yu, J.; Zhang, W.; Yang, Y.; Qian, G. A Ratiometric and Colorimetric Luminescent Thermometer over a Wide Temperature Range Based on a Lanthanide Coordination Polymer. *Chem. Commun.* **2014**, *50* (6), 719–721. https://doi.org/10.1039/c3cc47225f.

(36) Gálico, D. A.; Marin, R.; Brunet, G.; Errulat, D.; Hemmer, E.; Sigoli, F. A.; Moilanen, J. O.; Murugesu, M. Triplet-State Position and Crystal-Field Tuning in Opto-Magnetic Lanthanide Complexes: Two Sides of the Same Coin. *Chem. - A Eur. J.* **2019**, *25* (64), 14625–14637. https://doi.org/10.1002/chem.201902837.

(37) Lee, C. C.; MacKay, J. A.; Fréchet, J. M. J.; Szoka, F. C. Designing Dendrimers for Biological Applications. *Nat. Biotechnol.* **2005**, *23* (12), 1517–1526. https://doi.org/10.1038/nbt1171.

(38) Martinić, I.; Eliseeva, S. V.; Collet, G.; Luo, T. Y.; Rosi, N.; Petoud, S. One Approach for Two: Toward the Creation of Near-Infrared Imaging Agents and Rapid Screening of Lanthanide(III) Ion Sensitizers Using Polystyrene

Nanobeads. *ACS Appl. Bio Mater.* **2019**, *2* (4), 1667–1675. https://doi.org/10.1021/acsabm.9b00053.

(39) Karakoti, A. S.; Shukla, R.; Shanker, R.; Singh, S. Surface Functionalization of Quantum Dots for Biological Applications. *Adv. Colloid Interface Sci.* **2015**, *215*, 28–45. https://doi.org/10.1016/j.cis.2014.11.004.

(40) Cauzzi, D.; Pattacini, R.; Delferro, M.; Dini, F.; Di Natale, C.; Paolesse, R.; Bonacchi, S.; Montalti, M.; Zaccheroni, N.; Calvaresi, M.; Zerbetto, F.; Prodi, L. Temperature-Dependent Fluorescence of Cu 5 Metal Clusters: A Molecular Thermometer. *Angew. Chemie Int. Ed.* **2012**, *51* (38), 9662–9665. https://doi.org/10.1002/anie.201204052.

(41) Shamsieva, A. V.; Kolesnikov, I. E.; Strelnik, I. D.; Gerasimova, T. P.; Kalinichev, A. A.; Katsyuba, S. A.; Musina, E. I.; Lähderanta, E.; Karasik, A. A.; Sinyashin, O. G. Fresh Look on the Nature of Dual-Band Emission of Octahedral Copper-Iodide Clusters-Promising Ratiometric Luminescent Thermometers. *J. Phys. Chem. C* **2019**, *123* (42), 25863–25870. https://doi.org/10.1021/acs.jpcc.9b07603.

(42) Li, Y.; Li, Z.; Hou, Y.; Fan, Y. N.; Su, C. Y. Photoluminescent Phosphinine Cu(I) Halide Complexes: Temperature Dependence of the Photophysical Properties and Applications as a Molecular Thermometer. *Inorg. Chem.* **2018**, *57* (21), 13235–13245. https://doi.org/10.1021/acs.inorgchem.8b01732.

(43) Bünzli, J.-C.; Eliseeva, S. V. Basics of Lanthanide Photophysics. In *Lanthanide Luminescence: Photophysical, Analytical and Biological Aspects*; Springer-Verlag Berlin Heidelberg, 2011; pp 1–46. https://doi.org/10.1007/978-3-642-21023-5.

(44) Uha, H.; Petoud, S. Novel Antennae for the Sensitization of near Infrared Luminescent Lanthanide Cations. *Comptes Rendus Chim.* **2010**, *13* (6–7), 668–680. https://doi.org/10.1016/j.crci.2010.05.007.

(45) Deiters, E.; Song, B.; Chauvin, A. S.; Vandevyver, C. D. B.; Gumy, F.; Bünzli, J. C. G. Luminescent Bimetallic Lanthanide Bioprobes for Cellular Imaging with Excitation in the Visible-Light Range. *Chem. - A Eur. J.* **2009**, *15* (4), 885–900. https://doi.org/10.1002/chem.200801868.

(46) Gassner, A. L.; Duhot, C.; Bünzli, J. C. G.; Chauvin, A. S. Remarkable Tuning of the Photophysical Properties of Bifunctional Lanthanide Tris(Dipicolinates) and Its Consequence on the Design of Bioprobes. *Inorg. Chem.* **2008**, *47* (17), 7802–7812. https://doi.org/10.1021/ic800842f.

(47) Chauvin, A. S.; Comby, S.; Song, B.; Vandevyver, C. D. B.; Bünzli, J. C. G. A Versatile Ditopic Ligand System for Sensitizing the Luminescence of Bimetallic Lanthanide Bio-Imaging Probes. *Chem. - A Eur. J.* **2008**, *14* (6), 1726–1739. https://doi.org/10.1002/chem.200701357.

(48) Latva, M.; Takalob, H.; Mukkala, V. M.; Matachescu, C.; Rodríguez-Ubis, J. C.; Kankare, J. Correlation between the Lowest Triplet State Energy Level of the Ligand and Lanthanide(III) Luminescence Quantum Yield. *J. Lumin.* **1997**, *75* (2), 149–169. https://doi.org/10.1016/S0022-2313(97)00113-0.

(49) Archer, R. D.; Chen, H.; Thompson, L. C. Synthesis, Characterization, and Luminescence of Europium(III) Schiff Base Complexes. *Inorg. Chem.* **1998**, *37* (8), 2089–2095. https://doi.org/10.1021/ic960244d.

(50) Katagiri, S.; Tsukahara, Y.; Hasegawa, Y.; Wada, Y. Energy-Transfer Mechanism in Photoluminescent Terbium(III) Complexes Causing Their Temperature-Dependence. *Bull. Chem. Soc. Jpn.* **2007**, *80* (8), 1492–1503. https://doi.org/10.1246/bcsj.80.1492.

(51) Katagiri, S.; Hasegawa, Y.; Wada, Y.; Yanagida, S. Thermo-Sensitive Luminescence Based on the Back Energy Transfer in Terbium(III) Complexes. *Chem. Lett.* **2004**, *33* (11), 1438–1439. https://doi.org/10.1246/cl.2004.1438.

(52) Brites, C. D. S.; Lima, P. P.; Carlos, L. D. Tuning the Sensitivity of Ln3+-Based Luminescent Molecular Thermometers through Ligand Design. *J. Lumin.* **2016**, *169*, 497–502. https://doi.org/10.1016/j.jlumin.2015.01.025.

(53) Nguyen, T. N.; Chow, C. Y.; Eliseeva, S. V.; Trivedi, E. R.; Kampf, J. W.; Martinić, I.; Petoud, S.; Pecoraro, V. L. One-Step Assembly of Visible and Near-Infrared Emitting Metallacrown Dimers Using a Bifunctional Linker. *Chem. - A Eur. J.* **2018**, *24* (5), 1031–1035. https://doi.org/10.1002/chem.201703911.

(54) Jiang, X. F.; Chen, M. G.; Tong, J. P.; Shao, F. A Mononuclear Dysprosium(Iii) Single-Molecule Magnet with a Non-Planar Metallacrown. *New J. Chem.* **2019**, *43* (22), 8704–8710. https://doi.org/10.1039/c9nj01662g.

(55) CrysAlisPro 1.171.38.41. *Rigaku Oxford Diffr.* **2015**.

(56) CrystalClear Expert 2.0 R16. *Rigaku Am.* **2004**.

(57) Sheldrick, G. M. Crystal Structure Refinement with SHELXL. *Acta Crystallogr. Sect. C Struct. Chem.* **2015**, *71* (Md), 3–8. https://doi.org/10.1107/S2053229614024218.

(58) Spek, A. L. Structure Validation in Chemical Crystallography. *Acta Crystallogr. Sect. D Biol. Crystallogr.* **2009**, *65* (2), 148–155. https://doi.org/10.1107/S090744490804362X.

(59) Spek, A. L. Single-Crystal Structure Validation with the Program PLATON. *J. Appl. Crystallogr.* **2003**, *36* (1), 7–13. https://doi.org/10.1107/S0021889802022112.

(60) Martinić, I.; Eliseeva, S. V.; Nguyen, T. N.; Pecoraro, V. L.; Petoud, S. Near-Infrared Optical Imaging of Necrotic Cells by Photostable Lanthanide-Based Metallacrowns. *J. Am. Chem. Soc.* **2017**, *139* (25), 8388–8391. https://doi.org/10.1021/jacs.7b01587.

(61) Salerno, E. V.; Eliseeva, S. V.; Schneider, B. L.; Kampf, J. W.; Petoud, S.; Pecoraro, V. L. Visible, Near-Infrared, and Dual-Range Luminescence Spanning the 4f Series Sensitized by a Gallium(III)/Lanthanide(III) Metallacrown Structure. *J. Phys. Chem. A* **2020**, *124* (50), 10550–10564. https://doi.org/10.1021/acs.jpca.0c08819.

(62) Wang, J.; Lu, G.; Liu, Y.; Wu, S. G.; Huang, G. Z.; Liu, J. L.; Tong, M. L. Building Block and Directional Bonding Approaches for the Synthesis of {DyMn 4 } n (n = 2, 3) Metallacrown Assemblies. *Cryst. Growth Des.* **2019**, *19* (3), 1896–1902. https://doi.org/10.1021/acs.cgd.8b01879.

(63) Cirera, J.; Ruiz, E.; Alvarez, S. Continuous Shape Measures as a Stereochemical Tool in Organometallic Chemistry. *Organometallics* **2005**, *24* (7), 1556–1562. https://doi.org/10.1021/om049150z.

(64) Llunell, M.; Casanova, D.; Cicera, J.; Alemany, P.; Alvarez, S. Shape. Version 2.1. Barcelona, Spain 2013.

(65) Pagonis, V.; Ankjærgaard, C.; Murray, A. S.; Jain, M.; Chen, R.; Lawless, J.; Greilich, S. Modelling the Thermal Quenching Mechanism in Quartz Based on Time-Resolved Optically Stimulated Luminescence. *J. Lumin.* **2010**, *130* (5), 902–909. https://doi.org/10.1016/j.jlumin.2009.12.032.

(66) Hänninen, P.; Härmä, H. *Lanthanide Luminescence: Photophysical, Analytical and Biological Aspects*; Springer-Verlag Berlin Heidelberg, 2011. https://doi.org/10.1007/978-3-642-21023-5.

(67) Carneiro Neto, A. N.; Teotonio, E. E. S.; de Sá, G. F.; Brito, H. F.; Legendziewicz, J.; Carlos, L. D.; Felinto, M. C. F. C.; Gawryszewska, P.; Moura, R. T.; Longo, R. L.; Faustino, W. M.; Malta, O. L. Modeling Intramolecular Energy Transfer in Lanthanide Chelates: A Critical Review and Recent Advances; 2019; pp 55–162. https://doi.org/10.1016/bs.hpcre.2019.08.001.

(68) Samanta, P. K.; Kim, D.; Coropceanu, V.; Brédas, J.-L. Up-Conversion Intersystem Crossing Rates in Organic Emitters for Thermally Activated Delayed Fluorescence: Impact of the Nature of Singlet vs Triplet Excited States. *J. Am. Chem. Soc.* **2017**, *139* (11), 4042–4051. https://doi.org/10.1021/jacs.6b12124.

(69) Wang, L.; Ou, Q.; Peng, Q.; Shuai, Z. Theoretical Characterizations of TADF Materials: Roles of ΔG and the Singlet–Triplet Excited States Interconversion. *J. Phys. Chem. A* **2021**, *125* (7), 1468–1475. https://doi.org/10.1021/acs.jpca.0c09767.

(70) Suta, M.; Meijerink, A. A Theoretical Framework for Ratiometric Single Ion Luminescent Thermometers—Thermodynamic and Kinetic Guidelines for Optimized Performance. *Adv. Theory Simulations* **2020**, *3* (12), 1–32.

https://doi.org/10.1002/adts.202000176.

(71) Salerno, E. V.; Zeler, J.; Eliseeva, S. V.; Hernández-Rodríguez, M. A.; Carneiro Neto, A. N.; Petoud, S.; Pecoraro, V. L.; Carlos, L. D. [Ga3+8Sm3+2, Ga3+8Tb3+2] Metallacrowns Are Highly Promising Ratiometric Luminescent Molecular Nanothermometers Operating at Physiologically Relevant Temperatures. *Chem. - A Eur. J.* **2020**, *26* (61), 13792–13796. https://doi.org/10.1002/chem.202003239.

TOC artwork

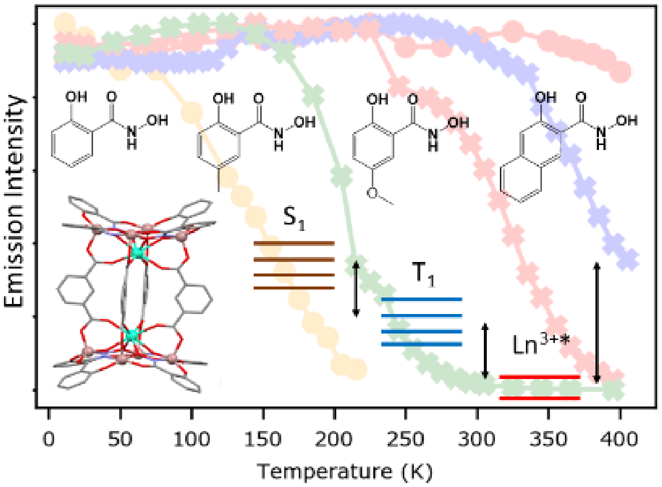

A novel family of optical molecular thermometers has been investigated photophysically and theoretically.